Adaptive and high-resolution estimation of specific differential phase for polarimetric X-band weather radars

Reinoso-Rondinel, Ricardo; Unal, Christine; Russchenberg, Herman

DOI
10.1175/JTECH-D-17-0105.1

Publication date
2018

Document Version
Final published version

Published in
Journal of Atmospheric and Oceanic Technology

Citation (APA)
Reinoso-Rondinel, R., Unal, C., & Russchenberg, H. (2018). Adaptive and high-resolution estimation of specific differential phase for polarimetric X-band weather radars. *Journal of Atmospheric and Oceanic Technology*, *35*(3), 555-573. https://doi.org/10.1175/JTECH-D-17-0105.1

Adaptive and High-Resolution Estimation of Specific Differential Phase for Polarimetric X-Band Weather Radars

RICARDO REINOSO-RONDINEL, CHRISTINE UNAL, AND HERMAN RUSSCHENBERG

Faculty of Civil Engineering and Geosciences, Delft University of Technology, Delft, Netherlands

(Manuscript received 8 June 2017, in final form 13 December 2017)

ABSTRACT

One of the most beneficial polarimetric variables may be the specific differential phase K_{DP} because of its independence from power attenuation and radar miscalibration. However, conventional K_{DP} estimation requires a substantial amount of range smoothing as a result of the noisy characteristic of the measured differential phase Ψ_{DP}. In addition, the backscatter differential phase δ_{hv} component of Ψ_{DP}, significant at C- and X-band frequency, may lead to inaccurate K_{DP} estimates. In this work, an adaptive approach is proposed to obtain accurate K_{DP} estimates in rain from noisy Ψ_{DP}, whose δ_{hv} is of significance, at range resolution scales. This approach uses existing relations between polarimetric variables in rain to filter δ_{hv} from Ψ_{DP} while maintaining its spatial variability. In addition, the standard deviation of the proposed K_{DP} estimator is mathematically formulated for quality control. The adaptive approach is assessed using four storm events, associated with light and heavy rain, observed by a polarimetric X-band weather radar in the Netherlands. It is shown that this approach is able to retain the spatial variability of the storms at scales of the range resolution. Moreover, the performance of the proposed approach is compared with two different methods. The results of this comparison show that the proposed approach outperforms the other two methods in terms of the correlation between K_{DP} and reflectivity, and K_{DP} standard deviation reduction.

1. Introduction

Weather observations are conventionally performed by single-polarization S- or C-band weather radars. Although these radars have substantially improved weather monitoring, researchers have found several limitations. For example, the spatial and temporal resolutions obtained from these conventional radars seem to be undesirable for the early detection of small but threatening features of convective weather as well as the detection of localized and heavy rainfall storms (Heinselman and Torres 2011; Schellart et al. 2012; Berne and Krajewski 2013). In contrast, single-polarization X-band weather radars are suited to obtain localized weather observations at resolutions higher than those of conventional radars. For example, a network of X-band weather radars in Hamburg, Germany, is used to observe precipitation at high resolutions (Lengfeld et al. 2016). Nonetheless, power attenuation and radar miscalibration may reduce the accuracy of single-polarization radar observables (Gourley et al. 2009).

One technique to potentially mitigate these issues is polarimetric radar technology (Doviak et al. 2000; Bringi and Chandrasekar 2001). For instance, in western Europe, polarimetric X-band weather radars are used to obtain high-resolution rainfall rates in order to cope with urban flooding (Ochoa-Rodriguez et al. 2015). In the United States, a network of X-band radars with polarimetric capabilities is used to improve the coverage of convective weather at low levels (McLaughlin et al. 2009), while in France a similar radar network is used to fill the gaps from operational radars in mountainous regions (Beck and Bousquet 2013). Moreover, in Germany, polarimetric Doppler X-band radars together with Doppler lidars are installed in international airports to provide local measurements of precipitation type and wind shear conditions, which are difficult to obtain from a national weather radar network (Ernsdorf et al. 2015).

In this work the polarimetric radar variable of interest is the specific differential phase K_{DP} because it is independent of attenuation and miscalibration; therefore, it can improve rainfall-rate estimation compared to power-based measurements, usually in heavy rain (Wang and Chandrasekar 2010). However, the accuracy

---

Corresponding author: Ricardo Reinoso-Rondinel, r.r.reinosorondinel@tudelft.nl

DOI: 10.1175/JTECH-D-17-0105.1

of K_{DP} is not yet sufficient because the measured differential phase Ψ_{DP} could be significantly noisy in light and moderate rain. In addition, in moderate and heavy rain, Ψ_{DP} can include a nonnegligible scattering component resulting from the Mie scattering region, which is known as the backscatter differential phase δ_{hv} (Matrosov et al. 2002; Trömel et al. 2013). Thus, accurate estimation of K_{DP} is necessary in order to unleash the potential of polarimetric weather radars.

Literature review reveals a large and continuous study to estimate K_{DP} and for simplicity it is divided into two groups. For the first group and in situations where δ_{hv} can be neglected (e.g., at S-band frequency or light rain), straightforward approaches based on autoregressive average models are applied to smooth Ψ_{DP} (Bringi and Chandrasekar 2001; Matrosov et al. 2006; Vulpiani et al. 2012). For the same group but in cases where δ_{hv} is of significance, Hubbert and Bringi (1995) introduced an iterative filtering approach to smooth Ψ_{DP} and filter δ_{hv}. A common problem in this group is that K_{DP} is estimated with inadequate spatial resolutions that could result in an underestimation of K_{DP} peaks and therefore lead to an inaccurate phase-based rainfall estimation (Ryzhkov and Zrnić 1996). This limitation was reduced by Wang and Chandrasekar (2009), who developed an algorithm to filter δ_{hv} and to control the smoothing degree on Ψ_{DP} while maintaining its spatial resolution. For the second group, the K_{DP} approaches included polarimetric relations in rain, such as the self-consistency (SC) relation, which formulates a dependency between K_{DP}, reflectivity Z, and differential reflectivity Z_{DR} (Scarchilli et al. 1996; Goddard et al. 1994; Gorgucci et al. 1992), and the relation between δ_{hv} and Z_{DR}, δ_{hv}–Z_{DR} (Scarchilli et al. 1993; Testud et al. 2000). Otto and Russchenberg (2011), were able to estimate K_{DP} at range resolution scales using both relations, while Schneebeli and Berne (2012) included the δ_{hv}–Z_{DR} relation in their Kalman filter approach. Recently, Giangrande et al. (2013) introduced a linear programming method that includes Z measurements, whereas Huang (2015) used the SC relation to estimate K_{DP} at S-, C-, and X-band frequencies. A disadvantage of using polarimetric relations is that uncertainties on Z and Z_{DR} measurements might reduce the performance of these approaches. Last, approaches in both groups could be associated with significant errors when K_{DP} is estimated at range resolution scales (Grazioli et al. 2014; Hu et al. 2015).

In this work an adaptive approach that includes polarimetric relations is presented to estimate accurate K_{DP} from Ψ_{DP} in rain, whose δ_{hv} is of significance, at high spatial resolution. This paper is a follow-up of Otto and Russchenberg (2011) and is organized as follows. Two K_{DP} methods—given by Hubbert and Bringi (1995), first group, and Otto and Russchenberg (2011), second group—are shortly described in section 2. They will be used for comparison with the proposed technique because (i) the method of Hubbert and Bringi (1995) is widely accepted for K_{DP} estimation at C- and X-band frequency and (ii) the focus of this work is to improve the technique introduced by Otto and Russchenberg (2011). In section 3, the adaptive high-resolution approach is introduced to estimate K_{DP} and model its standard deviation. To demonstrate the capability of this approach in terms of δ_{hv} contamination and spatial resolution, one storm event is analyzed in section 4. In section 5, the performance of the adaptive approach is compared with those from section 2, using four storm events. In section 6, conclusions are drawn. Finally, the standard deviation of the proposed K_{DP} estimator is derived in appendix A, while the filter required by Hubbert and Bringi (1995) is designed in appendix B.

2. Specific differential phase: Background and estimation

In polarimetric weather radars, the difference between the horizontal and vertical polarization phases is defined as Ψ_{DP} (°). A conceptual model for a Ψ_{DP} profile is expressed as

$$\Psi_{\mathrm{DP}}(r) = \Phi_{\mathrm{DP}}(r) + \delta_{\mathrm{hv}}(r) + \varepsilon, \tag{1}$$

where $\Phi_{\mathrm{DP}}(r)$ (°) represents the cumulative propagation phase shift along its course, while $\delta_{\mathrm{hv}}(r)$ (°) indicates local backscattering phase shifts manifested as "blips" or "bumps." Random noise is represented by ε (°) and the range by r (km). Depending on the weather environment, the standard deviation error of Ψ_{DP}, σ_P (°), varies between 2° and 5° (Bringi and Chandrasekar 2001).

The one-way K_{DP} (° km^{-1}) is half the derivative of Φ_{DP}:

$$K_{\mathrm{DP}}(r) = \frac{1}{2}\frac{d\Phi_{\mathrm{DP}}(r)}{dr}; \tag{2}$$

however, the estimation of accurate K_{DP} is not straightforward. For rainfall-rate applications, K_{DP} should be estimated such that the normalized standard error (NSE) of rainfall rate is less than 20% (Gorgucci et al. 1999; Bringi and Chandrasekar 2001). For instance, assuming a standard deviation of Φ_{DP} is equal to 3° and estimating K_{DP} as in Eq. (2) over a pathlength of 2 km, the standard deviation of K_{DP}, σ_K, would be 1° km^{-1}. If the rainfall rate and K_{DP} are given by a power-law relation with a power coefficient of 0.8 (Ryzhkov et al. 2005; Wang and Chandrasekar 2010), then the value of σ_K is theoretically sufficient for K_{DP} larger than 4° km^{-1}.

However, for K_{DP} values smaller than 4° km^{-1}, σ_K values are required to decrease accordingly, which can be achieved by increasing the pathlength with the sacrifice of spatial resolution.

a. Conventional method

Hubbert and Bringi (1995) introduced an iterative range filtering technique based on two steps. In the first step a low-pass filter is designed such that fluctuations resulting from δ_{hv} and ε at scales of the radar resolution [Δr (km)] are eliminated from the Ψ_{DP} profile. The magnitude response H of this filter is given in the range domain by defining its Nyquist frequency as $1/(2\Delta r)$. In this domain, H is specified by the filter order and $\Delta r/r_c$, where r_c (km) is the required cutoff scale such that $r_c > \Delta r$. This means that the filter will maintain (or "pass") spatial variations of $\Psi_{DP}(r)$ at scales larger than r_c. However, spatial variations smaller than r_c will not be effectively suppressed because H is characterized by a transition bandwidth from the "pass" band to the "stop" band. This transition can be faster if the order of the filter is heavily increased. However, a high-order filter will strongly smooth the spatial variability of Ψ_{DP}, leading to a coarse spatial resolution of K_{DP}. Thus, the order of the filter is selected such that H will suppress spatial variations at scales slightly larger than Δr without compromising the spatial resolution of K_{DP}. This filter is referred to as a "light" filter that will lead to reduced σ_P and thereby σ_K.

In the second step the light filter is applied several times to eliminate extended δ_{hv} fluctuations, up to r_c scales, as it would result from a "heavy" filter but without excessive smoothing. This process begins by filtering Ψ_{DP}, resulting in a first estimation of Φ_{DP} ($\tilde{\Phi}_{DP}$). The absolute difference between Ψ_{DP} and $\tilde{\Phi}_{DP}$ profiles at each range gate are employed to generate a modified Ψ_{DP} profile ($\tilde{\Psi}_{DP}$): if the absolute difference is larger than a threshold τ, then $\tilde{\Psi}_{DP}(r) = \tilde{\Phi}_{DP}(r)$ holds; otherwise, $\tilde{\Psi}_{DP}(r) = \Psi_{DP}(r)$ holds. This threshold is predefined from the interval $[1.25; 2]\sigma_P$. The process is iterated until $\tilde{\Psi}_{DP}$ from two consecutive iterations show insignificant changes. Next, $\tilde{\Psi}_{DP}$ from the last iteration is filtered one more time to obtain Φ_{DP} and thereby K_{DP} according to Eq. (2).

Even though this is an elegant approach to estimate K_{DP} in real time, the following issues limit its purpose. First, spatial fluctuations larger than r_c will not be completely eliminated by the iterative step. Second, its performance is sensitive to the value of τ. For example, $\tau = 2\sigma_P$ will lead to a $\tilde{\Psi}_{DP}$ more correlated to Ψ_{DP} than to $\tilde{\Phi}_{DP}$, which might not be sufficient to eliminate unwanted fluctuations. Third, if r_c is increased or Δr is decreased, then the order of the filter should be increased (Wang and Chandrasekar 2009), which may exacerbate these issues. In summary, in the design of the filter and the selection of the threshold, there is a tradeoff between the smoothing extent and the spatial resolution required to estimate K_{DP} with small standard deviation and reduced bias.

b. High-resolution method

In contrast to the conventional approach, Otto and Russchenberg (2011) included δ_{hv}–Z_{DR} and SC relations in rain to estimate K_{DP} at X-band frequency. The first relation is represented by $\delta_{hv} = e_1 Z_{DR}^{e_2}$ and the second by

$$K_{DP}^{SC} = c_1 10^{(c_2 Z/10)} 10^{(c_3 Z_{DR})}, \qquad (3)$$

where Z and Z_{DR} are given in dBZ and decibels (dB), respectively, while coefficients e_1, e_2, c_1, c_2, and c_3 establish the average fit from a set of drop size distributions (DSDs), drop shape models, and temperatures. The specific differential phase in Eq. (3) is indicated by K_{DP}^{SC} to distinguish between K_{DP} from the SC relation and K_{DP} from the high-resolution approach. Otto and Russchenberg (2011) used a normalized gamma distribution to model DSDs. To represent rain variability, 1500 DSDs were modeled by varying the parameters of the distribution (i.e., median volume diameter, concentration, and shape parameter). In addition, a hybrid drop shape model that consists of three models and temperatures in the range of 1°–25°C was considered to express a wide range of possibilities. The coefficients for the δ_{hv}–Z_{DR} relation are $e_1 = 1$ and $e_2 = 1.8$, while for the SC relation they are $c_1 = 1.37 \times 10^{-3}$, $c_2 = 0.68$, and $c_3 = -0.042$.

The measurements for Z and Z_{DR} are corrected for attenuation and differential attenuation, respectively, according to Bringi et al. (1990). The path-integrated attenuation (PIA) in reflectivity and in differential reflectivity (PIA_{DP}) is given by $0.34\Delta\Psi_{DP}$ and $0.05\Delta\Psi_{DP}$, respectively, where both coefficients are obtained from scattering simulation. For a Ψ_{DP} profile represented by Eq. (1), the difference of Ψ_{DP} in a path $\overline{ab}$ can be approximated as $\Delta\Psi_{DP} = \Delta\Phi_{DP} + \Delta\delta_{hv}$, where $\Delta\Psi_{DP} = \Psi_{DP}(b) - \Psi_{DP}(a)$ and $b > a$. The length of $\overline{ab}$ could be as small as Δr or as large as the maximum unambiguous range. To identify whether $\Delta\delta_{hv}$ is negligible, the δ_{hv}–Z_{DR} relation is used in the following assumption: if $|Z_{DR}(b) - Z_{DR}(a)|$ is smaller than 0.3 dB, then $\delta_{hv}(b) - \delta_{hv}(a) \approx 0°$. If that case is satisfied, then $\Delta\Psi_{DP}$ is retained for further processes; otherwise, $\Delta\Psi_{DP}$ is discarded. Multiple $\Delta\Psi_{DP}$ samples associated with negligible $\Delta\delta_{hv}$ are obtained by considering more paths. These samples are weighted by Z and Z_{DR} using the SC relation to obtain $\Delta\Psi_{DP}$ samples at Δr scale. For instance, the weight w at gate i within path $\overline{ab}$ is

$$w(i)=\frac{K_{\mathrm{DP}}^{\mathrm{SC}}(i)}{\sum_{a}^{b}K_{\mathrm{DP}}^{\mathrm{SC}}(g)};\quad \text{with}\quad g=a,\ldots,b. \tag{4}$$

Weighted $\Delta\Psi_{\mathrm{DP}}$ samples are used according to Eq. (2) to obtain multiple K_{DP} samples. Finally, $K_{\mathrm{DP}}(i)$ is estimated by the arithmetic mean of these samples.

Otto and Russchenberg (2011) demonstrated their method using one rainfall event, showing a visual consistency between K_{DP} and Z as well as between δ_{hv} and Z_{DR}. Nevertheless, fewer consistent results were observed for K_{DP} values smaller than 4° km^{-1}. In addition, estimates of K_{DP} were associated with values of σ_K as high as 3° km^{-1}. Moreover, the sensitivity of the SC relation to DSD, drop shape, and temperature variability and its impact on estimated weights were not discussed. In addition, the effect of uncertain measurements of Z and Z_{DR} caused by, for example, attenuation, partial beam blockage (PBB), and miscalibration on the performance of this approach remains an open question. Besides its limited validation, another matter is the computational time required to weigh a significant amount of $\Delta\Psi_{\mathrm{DP}}$ samples at each range gate, which might be inefficient for operational purposes.

3. Adaptive high-resolution approach

The presented approach is an improved version of the high-resolution method in order to address limitations associated with the conventional and high-resolution methods, mainly the low accuracy of K_{DP} in light rain, contamination resulting from unfiltered δ_{hv}, sensitivity to Z and Z_{DR} measurements, and computational time. The inputs are radial measurements of Ψ_{DP}, Z, and Z_{DR} in rain. In addition, a predetermined length interval $[L_{\min};\ L_{\max}]$ is required to control the selection of pathlengths. This interval is assumed to be defined by a user; however, possible values are discussed in section 3e. The adaptive approach consists of three processes: preprocessing, pathlength selection, and K_{DP} estimation. A flowchart to estimate K_{DP}, among other variables, for a given radial profile, is presented in Fig. 1.

a. Preprocessing

To correct Z and Z_{DR} profiles for attenuation and differential attenuation, respectively, Otto and Russchenberg (2011) used noisy $\Delta\Psi_{\mathrm{DP}}$ instead of $\Delta\Phi_{\mathrm{DP}}$, which may decrease the accuracy of the method given by Bringi et al. (1990). In contrast, in the adaptive high-resolution approach, a linear regression fit over a 3-km window is applied to a Ψ_{DP} profile, resulting in a Φ_{DP} profile (Φ_{DP}^t). Thus, attenuation-corrected reflectivity (Z^t) and differential reflectivity (Z_{DR}^t) are given as $Z^t = z + 0.34\Delta\Phi_{\mathrm{DP}}^t$ and $Z_{\mathrm{DR}}^t = z_{\mathrm{dr}} + 0.05\Delta\Phi_{\mathrm{DP}}^t$, respectively, where z (dBZ) and z_{dr} (dB) represent attenuated and differential attenuated measurements, respectively. This attenuation correction method might be sensitive to measurements errors, constant coefficients, and δ_{hv} contamination. However, Gorgucci and Chandrasekar (2005) studied the method of Bringi et al. (1990) at X-band frequency and showed that this method performs fairly well with only a slight degradation of the average error for attenuation correction.

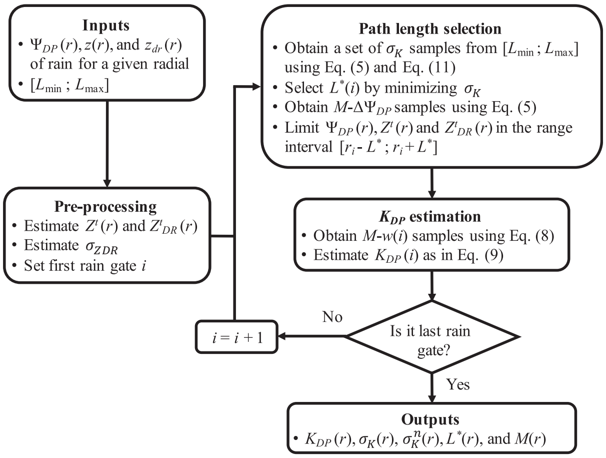

FIG. 1. Flowchart for the adaptive high-resolution K_{DP} approach.

In this approach an estimate of the standard deviation of Z_{DR}^t profile, σ_{ZDR} (dB), is required by the pathlength selection process. A moving window of five gates is applied to the Z_{DR}^t profile so that local σ_{ZDR} samples are obtained. Then, σ_{ZDR} is estimated by averaging these σ_{ZDR} samples. The estimation of K_{DP} is achieved gate by gate, starting from ranges near the radar and continuing downrange. Assuming that the first gate with measurements of rain is located at r_i, the estimation of K_{DP} begins at gate i.

b. Pathlength selection

In the high-resolution technique, $\Delta\Psi_{\mathrm{DP}}$ samples were obtained from Ψ_{DP} using paths of any possible length. However, K_{DP} results were associated with high values of σ_K and significant computational time. In this work a pathlength L (km) for gate i is selected from $[L_{\min};\ L_{\max}]$ such that a theoretical σ_K is minimized. The formulation of a theoretical σ_K is shown in section 3e but now let the theoretical σ_K be a function of parameters L and M, where M represents the number of $\Delta\Psi_{\mathrm{DP}}$ samples with negligible $\Delta\delta_{\mathrm{hv}}$. To identify negligible $\Delta\delta_{\mathrm{hv}}$, the high-resolution technique used a fixed threshold to constrain $|\Delta Z_{\mathrm{DR}}^t|$. However, a fixed threshold might not capture the possible variability of Z_{DR} within the storm. In this work the condition to identify negligible $\Delta\delta_{\mathrm{hv}}$ is given by

$$|\Delta Z_{\mathrm{DR}}^{t}| < \sigma_{\mathrm{ZDR}}. \tag{5}$$

Equation (5) can be considered to be independent of any parameterized δ_{hv}–Z_{DR} relation because this relation is not used quantitatively. Instead, Eq. (5) relies on the existing correlation between δ_{hv} and Z_{DR}. Furthermore, the sudden variability in microphysics is taken into consideration by using σ_{ZDR} rather than an arbitrary threshold. Issues such as Z_{DR} miscalibration are mitigated by the estimation of $\Delta Z_{\mathrm{DR}}^{t}$. Equation (5) is referred to as the $\Delta\Psi_{\mathrm{DP}}$ filter condition.

The pathlength selection starts with $L = L_{\min}$. For simplicity, a pathlength is of the form $L = n\Delta r$, where n is an integer larger than 1. Then, a range interval centered at gate i is defined as $[r_i - L; r_i + L]$. This range interval is used to limit the extent of Z_{DR}^{t} and to obtain multiple $\Delta Z_{\mathrm{DR}}^{t}$ samples. These samples are achieved by shifting a path of length L, within the interval starting at $r_i - L$, n times with steps of Δr. In this manner, $(n + 1)$–$\Delta Z_{\mathrm{DR}}^{t}$ samples are obtained. Next, M is calculated by counting the number of samples that satisfy Eq. (5). Note that $M \leq (n + 1)$. From L and M, a σ_K value is determined. To have a set of σ_K values, the same procedure is repeated for the next value of L until $L = L_{\max}$. Finally, the pathlength that leads to the minimum σ_K is selected and is represented by L^*.

Repeating a similar procedure but with L^* [i.e., shifting a path of length L^* and using Eq. (5)], M–$\Delta\Psi_{\mathrm{DP}}$ samples with negligible $\Delta\delta_{\mathrm{hv}}$ are retrieved from Ψ_{DP} to estimate $K_{\mathrm{DP}}(i)$. The remaining $\Delta\Psi_{\mathrm{DP}}$ samples are discarded to avoid bias on $K_{\mathrm{DP}}(i)$. For the next steps, only Ψ_{DP}, Z^t, and Z_{DR}^{t} profiles in the interval $[r_i - L^*; r_i + L^*]$ are used.

c. K_{DP} *estimation*

To estimate $K_{\mathrm{DP}}(i)$, M–$\Delta\Psi_{\mathrm{DP}}$ samples should be downscaled from L^* to Δr scales. A downscaling weight $w(i)$ was suggested by the high-resolution method according to Eq. (4). In contrast, in the adaptive high-resolution approach, a different formulation of $w(i)$ is proposed in order to reduce its sensitivity to possible sources of uncertainty that were discussed in section 2b, mainly the sensitivity of the SC relation to rain variability, radar miscalibration, and PBB effects. Moreover, this formulation allows us to study statistics of $w(i)$ and $K_{\mathrm{DP}}(i)$ for quality control purposes.

Consider a theoretical $\Delta\Psi_{\mathrm{DP}} \geq 0°$ from a path $\overline{ab}$ of length L. For gate i in the interval $[a + 1; b]$, the downscaling weight $w(i)$ is expressed as a factor that weighs $\Delta\Psi_{\mathrm{DP}}$ such that $\Delta\Psi_{\mathrm{DP}}(i) = w(i)\Delta\Psi_{\mathrm{DP}}$, where $\Delta\Psi_{\mathrm{DP}}(i)$ represents the difference $\Psi_{\mathrm{DP}}(i) - \Psi_{\mathrm{DP}}(i - 1)$ (i.e., at Δr scale). For derivation purposes, let $w(i)$ be bounded by the interval [0; 1] and $\sum_{a+1}^{b} w(i) = 1$. Using Eqs. (1) and (2), $\Delta\Psi_{\mathrm{DP}}(i)$ and $\Delta\Psi_{\mathrm{DP}}$ are expressed in terms of K_{DP} and $w(i)$ as

$$w(i) = \frac{2\Delta r K_{\mathrm{DP}}(i) + \delta_{\mathrm{hv}}(i) - \delta_{\mathrm{hv}}(i-1)}{2LK_{\mathrm{DP}} + \delta_{\mathrm{hv}}(b) - \delta_{\mathrm{hv}}(a)}. \tag{6}$$

Both $K_{\mathrm{DP}}(i)$ and K_{DP} are estimated using the SC relation according to Eq. (3) at scales of Δr and L, respectively. In the numerator of Eq. (6), adjacent δ_{hv} values are assumed to be similar, so $\delta_{\mathrm{hv}}(i) - \delta_{\mathrm{hv}}(i - 1)$ is approximately 0°. In the denominator, assuming that $\Delta\Psi_{\mathrm{DP}}$ satisfies Eq. (5), the difference $\delta_{\mathrm{hv}}(b) - \delta_{\mathrm{hv}}(a)$ is negligible. In this manner, $w(i)$ is formulated as

$$w(i) = \frac{\Delta r}{L}\frac{K_{\mathrm{DP}}^{\mathrm{SC}}(i)}{K_{\mathrm{DP}}^{\mathrm{SC}}}, \tag{7}$$

where the SC relation is used two times in contrast to the high-resolution method, which is used $(n + 2)$ times [see Eq. (4) and replace b with $a + n$]. In this way, added errors associated with the SC relation are reduced.

To downscale M–$\Delta\Psi_{\mathrm{DP}}$ samples (i.e., $\Delta\Psi_{\mathrm{DP}}^{(j)}$ with $j = 1, 2, \ldots M$) associated with M–$\overline{ab}$ paths of length L^*, Eq. (7) is used and the jth weight is given as

$$\hat{w}^{(j)}(i) = \frac{\Delta r}{L^*}10^{c_2[Z^t(i) - \overline{Z}^{(j)}]/10}10^{c_3[Z_{\mathrm{DR}}^{t}(i) - \overline{Z}_{\mathrm{DR}}^{(j)}]}, \tag{8}$$

where $\overline{Z}^{(j)}$ and $\overline{Z}_{\mathrm{DR}}^{(j)}$ represent the arithmetic mean of $Z^t(i)$ and $Z_{\mathrm{DR}}^{t}(i)$ values in path $\overline{ab}^{(j)}$, respectively. Repeating Eq. (8) over the remaining paths, M–$\hat{w}(i)$ samples are obtained and $K_{\mathrm{DP}}(i)$ is estimated as

$$\hat{K}_{\mathrm{DP}}(i) = \frac{1}{M}\sum_{j=1}^{M}\frac{\Delta\Psi_{\mathrm{DP}}^{(j)}\hat{w}^{(j)}(i)}{2\Delta r}; \quad \text{with} \quad j = 1, 2, \ldots M. \tag{9}$$

Once $K_{\mathrm{DP}}(i)$ is estimated, the pathlength selection and K_{DP} estimation processes are applied to gate $i = i + 1$ until the last gate measured in rain. Hence, a K_{DP} profile is obtained as well as associated L^* and M profiles.

d. K_{DP} *uncertainty*

The K_{DP} estimator is a function of variables $\Delta\Psi_{\mathrm{DP}}^{(j)}$ and $\hat{w}^{(j)}$, which result from the $\Delta\Psi_{\mathrm{DP}}$ filter condition and $\Delta\Psi_{\mathrm{DP}}$ downscaling, respectively. Therefore, it is important to discuss errors associated with both variables. For this purpose, $\Delta\Psi_{\mathrm{DP}}^{(j)}$ is expressed as $\Delta\Psi_{\mathrm{DP}} = \Delta\Phi_{\mathrm{DP}} + \varepsilon_\delta$, where ε_δ indicates possible errors from neglecting $\Delta\delta_{\mathrm{hv}}$. Using the scattering simulation introduced in section 2b and setting σ_{ZDR} equal to 0.2 dB, the estimated mean and standard deviation of ε_δ are 0.04° and 0.6°, respectively. The uncertainty of $\hat{w}^{(j)}$ depends on the SC relation in rain. Trabal et al. (2014) demonstrated that the coefficients of the SC relation shown in Eq. (3) are sensitive to temperature variability, while DSD and drop shape variabilities are well represented by a normalized gamma distribution and a hybrid drop shape model. Similar findings were reported by Gourley et al. (2009) and Adachi et al. (2015). Although $\hat{w}^{(j)}$ is independent of c_1, any possible sensitivity to c_2 and c_3 is modulated by the difference $Z^t(i) - \overline{Z}^{(j)}$ and $Z^t_{\mathrm{DR}}(i) - \overline{Z}^{(j)}_{\mathrm{DR}}$, respectively (i.e., it depends on the spatial variability of Z^t and Z^t_{DR} within path $\overline{ab}^{(j)}$ instead of their absolute values). For example, in a uniform path, $\hat{w}^{(j)}$ might be constant and equal to $\Delta r/L^*$. Moreover, $\hat{w}^{(j)}$ is independent of constant biases in Z^t and Z^t_{DR} within $\overline{ab}^{(j)}$ as well as radar miscalibration. This independence could reduce the impact of biases on Z^t and Z^t_{DR} areas caused by PBB. For simplicity the estimated weight is rewritten as $\hat{w}^{(j)} = \hat{\alpha}^{(j)}\Delta r/L$, where $\hat{\alpha}^{(j)}$ is referred to as the SC ratio [see Eqs. (7) and (8)].

The uncertainty of $\hat{\alpha}^{(j)}$ can be quantified by its NSE. Scarchilli et al. (1996) derived an expression for NSE of $K^{\mathrm{SC}}_{\mathrm{DP}}$, hereinafter NSE($K$), that is a function of c_2, c_3, and variances of Z^t and Z^t_{DR}. Using this expression and basic properties of the variance, the NSE of $\hat{\alpha}^{(j)}$ is given by $\mathrm{NSE}[\hat{\alpha}^{(j)}] = \sqrt{1+1/n}\,\mathrm{NSE}(K)$. For example, setting n equal to 10 (i.e., L is 10 times Δr) and using values of c_2 and c_3 given in section 2b and conventional accuracies of 1 and 0.2 dB for Z^t and Z^t_{DR}, respectively, $\mathrm{NSE}[\hat{\alpha}^{(j)}]$ results in 15.7%. This analysis can be used as guidance to identify which elements associated with the $\Delta\Psi_{\mathrm{DP}}$ filter condition and $\Delta\Psi_{\mathrm{DP}}$ downscaling can lead to an incorrect estimation of K_{DP}.

The uncertainty of $\hat{K}_{\mathrm{DP}}(i)$ is measured by its standard deviation as

$$\sigma_K(i) = \sqrt{\frac{1}{M}\sum_{j=1}^{M}\left[\frac{\Delta\Psi^{(j)}_{\mathrm{DP}}\,\hat{w}^{(j)}(i)}{2\Delta r} - \hat{K}_{\mathrm{DP}}(i)\right]^2}; \quad \text{with} \quad j = 1, 2, \ldots M. \tag{10}$$

Equation (10) is referred to as the actual σ_K. In addition, the NSE of $\hat{K}_{\mathrm{DP}}(i)$, hereinafter $\sigma^n_K(i)$, is given by $[\sigma_K(i)/|\hat{K}_{\mathrm{DP}}(i)|]100\%$. Both actual σ_K and σ^n_K profiles are added to the output of Fig. 1, which can be used for quality control purposes. In a similar manner but for the M–$\hat{\alpha}(i)$ samples, profiles of their actual mean (μ_α), standard deviation (σ_α), and NSE (σ^n_α) are also obtained.

e. σ_K modeling

The uncertainty of $\hat{K}_{\mathrm{DP}}$ can be controlled by modeling its actual σ_K. Therefore, a theoretical σ_K is derived from Eq. (9), where $\hat{w}^{(j)}$ is replaced by $\hat{\alpha}^{(j)}\Delta r/L$. Values of Δr, L, and M are assumed to be given, while $\Delta\Psi^{(j)}_{\mathrm{DP}}$ and $\hat{\alpha}^{(j)}$ are defined as random variables. Using properties of the variance that involve the sum and product of random variables, a theoretical σ_K is approximated as (for a detailed derivation, refer to appendix A)

$$\sigma_K = \frac{\mu_\alpha}{L}\sqrt{\frac{2\sigma_P^2 + \sigma_\varepsilon^2}{4M}}, \tag{11}$$

where σ^2_P and σ^2_ε are the variance of Ψ_{DP} and ε_δ, respectively. The value of μ_α depends on the spatial variability of Z^t and Z^t_{DR}. For example, μ_α may be near 1 in stratiform rain, but it can be between 2 and 5 in convective rain. The value of σ_P also depends on rain type, while σ_ε is assumed equal to 0.6° as given in section 3d. To illustrate theoretical σ_K, let us assume that μ_α and σ_P are equal to 3 and 3°, respectively. A similar value for σ_P was given by Lim et al. (2013).

Theoretical σ_K curves as a function of M and for different combinations of L are presented in Fig. 2. Although σ_K in Eq. (11) is independent of Δr, the maximum value of M for a fixed pathlength L is given by $(n + 1)$, which is equivalent to $L/\Delta r + 1$. For Δr equal to 0.03 km, Fig. 2a shows that if L is near 1 km, then it is expected to obtain σ_K values larger than 1° km^{-1}. However, σ_K values smaller than 0.5° km^{-1} are expected if L is equal to 2 km and M is larger than 40. In terms of probability, M larger than 40 indicates that at least 60% of the total number of paths $(n + 1)$ satisfies Eq. (5). For L larger than 3 km, σ_K curves continue for values of M beyond 100 but are not shown here. Note that the gap between consecutive σ_K curves decreases as L increases (e.g., σ_K curves corresponding to 5 and 6 km are almost identical). Therefore, it is recommended to avoid large values of L (i.e., lengthy paths) associated with a small reduction of σ_K.

Recall that for a given value of L, M is determined only after evaluating Eq. (5). To search for the combination of L and M that leads to the smallest theoretical σ_K, a pathlength interval [$L_{\min}$; $L_{\max}$] is considered instead of a single pathlength. For example, a length interval equal to [3;5] km could be defined from Fig. 2a as an input to the adaptive high-resolution approach. In that case, σ_K is expected to be small with a sufficient number of paths M. Similar σ_K curves can be produced for a coarser spatial resolution. For instance, if Δr = 0.25 km, then a set of L values ranging from 4 to 14 km would be used to generate σ_K curves as shown in Fig. 2b and an interval equal to [6;10] km would be defined. Note that for larger Δr, a smaller number of paths M might lead to reasonable σ_K values (cf. Figs. 2a and 2b).

In this σ_K modeling, it is assumed that a user predefines a theoretical value for μ_α and σ_P according to the storm type, and sets [$L_{\min}$; $L_{\max}$]. For example, in a uniform Z field (i.e., low μ_α and σ_P) or a more variable Z field (i.e., high μ_α and σ_P), [$L_{\min}$; $L_{\max}$] can be decreased

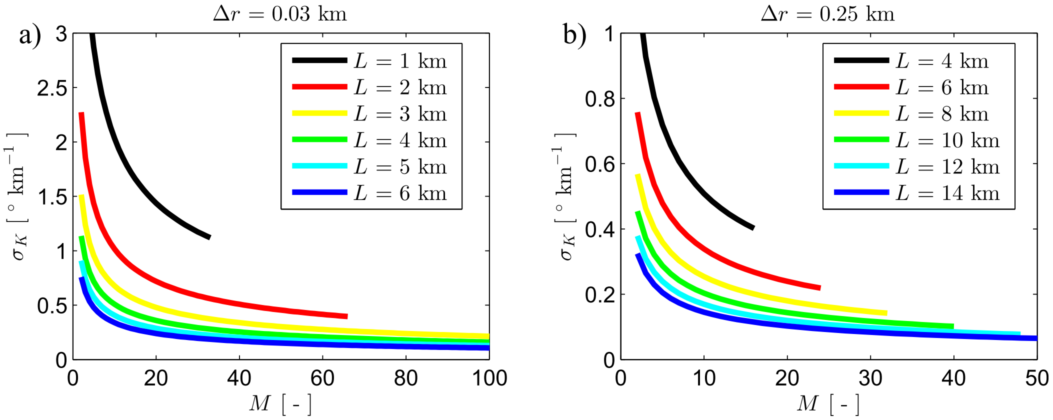

FIG. 2. Theoretical standard deviation of the adaptive high-resolution K_{DP} estimator as a function of the number of paths M. (a) Theoretical σ_K curves for $\mu_\alpha = 3$ and $\Delta r = 0.03$ km. (b) As in (a), but for $\Delta r = 0.25$ km.

or increased according to theoretical σ_K curves. In summary, setting $[L_{\min}; L_{\max}]$ allows us to avoid high values of actual σ_K as well as unnecessary lengthy paths associated with an increased dependence on the SC ratio and a large computational time.

4. Analysis of the adaptive high-resolution approach

a. Data settings

The polarimetric X-band weather radar the International Research Centre for Telecommunications and Radar (IRCTR) drizzle radar (IDRA) is a frequency-modulated continuous wave system whose operational range is 15.3 km with a resolution of 0.03 km (Figueras i Ventura 2009). IDRA is located at the Cabauw Experimental Site for Atmospheric Research (CESAR) observatory in the Netherlands at a height of 213 m from ground level (Leijnse et al. 2010). It scans at a fixed elevation of 0.50° and rotates the antenna over 360° in 1 min with a beamwidth of 1.8°. Clutter echoes are removed by a filter based on spectral polarimetric processing (Unal 2009). Moreover, the measured linear depolarization ratio L_{DR} is used to filter areas that include particles other than rain and have low SNR, such that range gates with L_{DR} larger than −18 dB are removed (Bringi and Chandrasekar 2001). This simple filtering procedure should be extended in the case of an automatic algorithm. The unwrapping of differential phase profiles is performed by detecting a differential phase jump between two adjacent gates, equal to 80% of the maximum differential phase of 180°.

A convective storm event was observed by IDRA on 10 September 2011. The plan position indicators (PPIs) of z, z_{dr}, and Ψ_{DP} are shown in Fig. 3. Attenuation-affected areas can be identified behind strong reflectivity echoes. The radial pattern observed in the fields of z_{dr} and Ψ_{DP} is probably due to a metallic fence that surrounds the IDRA platform. This introduces an azimuthal-dependence bias in the z_{dr} field in a similar way as PBB effects (Giangrande and Ryzhkov 2005). In addition, z might suffer from radar miscalibration as reported by Otto and Russchenberg (2011). Here, we use the opportunity to study the impact of rain attenuation and biases associated with PBB and miscalibration on the adaptive high-resolution approach.

b. Methodology

The proposed K_{DP} approach is analyzed using the storm event observed by IDRA. Besides the z, z_{dr}, and Ψ_{DP} fields, a pathlength interval is required. For this requirement, Fig. 2a can be used for guidance because the theoretical σ_K curves were built for the same range resolution as for IDRA and with theoretical μ_α and σ_P equal to 3 and 3°, respectively, which express the spatial variability of the observed z and Ψ_{DP} fields. Thus, from Fig. 2a, a length interval of [3;5] km, which is associated with $\sigma_K < 0.5°\,\mathrm{km}^{-1}$ for $M > 20$, is selected. This interval is used by the pathlength selection process for all radials. For simplicity, $L^*(i)$ is indicated by $L(i)$ and is determined by minimizing $1/(L\sqrt{4M})$ instead of σ_K, as shown by Eq. (11), because theoretical μ_α, σ_P, and σ_ε remain constant in all radials. The coefficients c_2 and c_3 given in section 2b are used by the K_{DP} estimation process.

To study the performance of the K_{DP} approach in terms of spatial resolution and δ_{hv} filtering, three variations on applying the $\Delta\Psi_{DP}$ filter condition and $\Delta\Psi_{DP}$ downscaling, given by Eqs. (5) and (9) respectively, are defined and indicated in Table 1. In case I, K_{DP} is estimated using the $\Delta\Psi_{DP}$ filter condition without

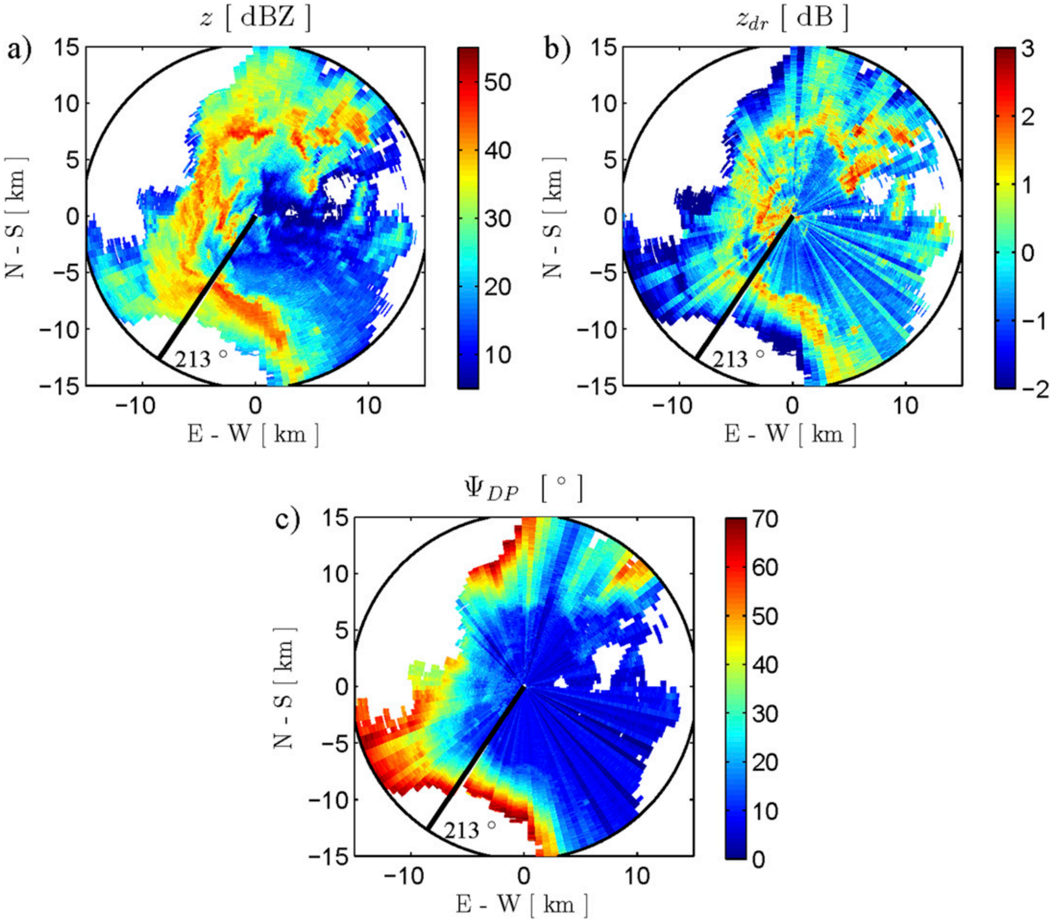

FIG. 3. Observations by the IDRA radar at an elevation angle of 0.5° in the Netherlands at 1950 UTC 10 Sep 2011. Fields of (a) attenuated reflectivity, (b) attenuated differential reflectivity, and (c) differential phase. Also shown is the 15.3-km range coverage of IDRA (black circles). Range resolution is 0.03 km.

downscaling $\Delta\Psi_{\mathrm{DP}}^{(j)}$ (i.e., $\hat{w}^{(j)} = \Delta r/L$ and the SC ratio is equal to 1). This case is denoted by $\Delta\delta_{\mathrm{hv}} \approx 0°$ and $\alpha \approx 1$. In case II, the $\Delta\Psi_{\mathrm{DP}}$ filter condition is not used but $\Delta\Psi_{\mathrm{DP}}^{(j)}$ is downscaled. This case is expressed by $\Delta\delta_{\mathrm{hv}} \neq 0°$ and $\alpha \neq 1$. In case III, the $\Delta\Psi_{\mathrm{DP}}$ filter condition is applied and $\Delta\Psi_{\mathrm{DP}}^{(j)}$ is downscaled, and this case is represented by $\Delta\delta_{\mathrm{hv}} \approx 0°$ and $\alpha \neq 1$. Note that case III follows the proposed K_{DP} approach and that cases I and II are defined only for analysis purposes.

After a K_{DP} profile is obtained, a Φ_{DP} profile is reconstructed by integrating Eq. (2) and δ_{hv} is determined as $\delta_{\mathrm{hv}} = \Psi_{\mathrm{DP}} - \Phi_{\mathrm{DP}}$. Moreover, Z and Z_{DR} are obtained by correcting z and z_{dr} in a similar manner as in section 3a but replacing $\Delta\Phi_{\mathrm{DP}}^{t}$ with $\Delta\Phi_{\mathrm{DP}}$. This correction method could be improved by using more sophisticated techniques, such as those given by Park et al. (2005a) and Snyder et al. (2010). However, attenuation correction for z and z_{dr} is beyond the scope of this work, as our goal is to assess the performance of the K_{DP} approach.

c. K_{DP} and σ_K results

1) FOR A PPI RADIAL

The K_{DP} approach specified by cases I–III is applied to the azimuthal radial of 213° and its results are shown in Fig. 4. The downscaling aspect of K_{DP} is examined by comparing the Ψ_{DP}, Φ_{DP} (case I), and Φ_{DP} (case III) profiles as shown in Fig. 4a. Observe that the total $\Delta\Phi_{\mathrm{DP}}$ for cases I and III is equal to 45°. However, Φ_{DP} from case III captures the spatial variability and rapid increments of Ψ_{DP} better than Φ_{DP} from case I. This can be seen by their corresponding K_{DP} profiles, which are also shown in Fig. 4a but they are shifted by $-10°\,\mathrm{km}^{-1}$, where two K_{DP}

TABLE 1. Three cases for K_{DP} estimation using the adaptive HR approach.

Cases	I	II	III
$\Delta\delta_{\mathrm{hv}}$	$\Delta\delta_{\mathrm{hv}} \approx 0°$	$\Delta\delta_{\mathrm{hv}} \neq 0°$	$\Delta\delta_{\mathrm{hv}} \approx 0°$
α	$\alpha \approx 1$	$\alpha \neq 1$	$\alpha \neq 1$

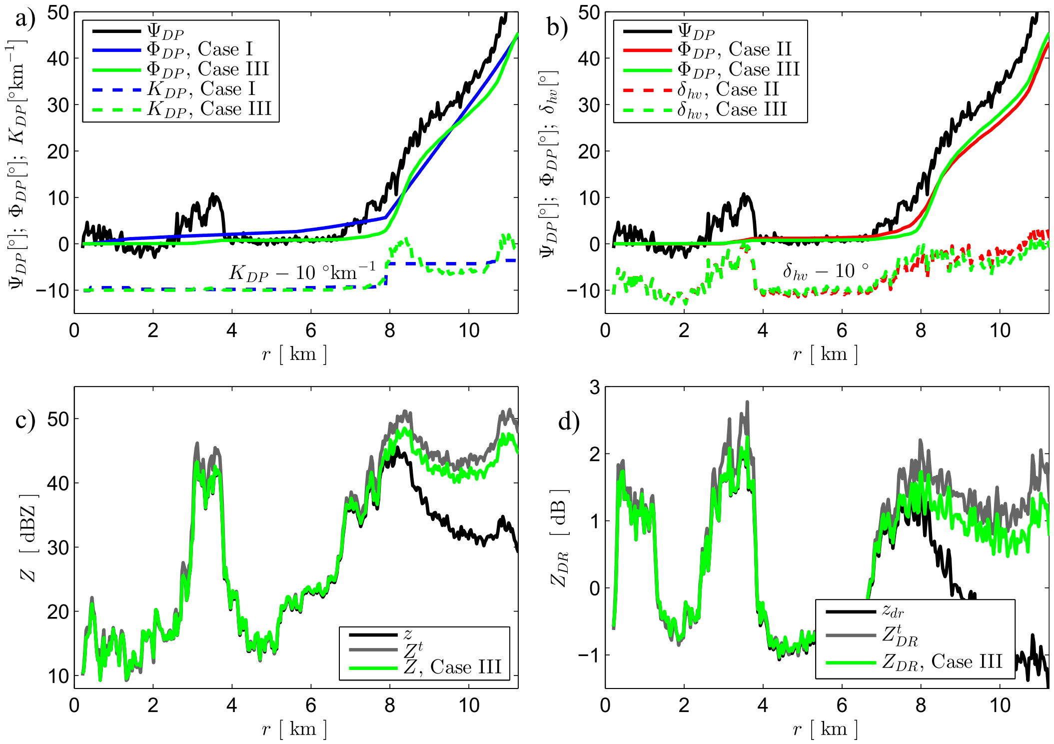

FIG. 4. Profiles from estimating K_{DP} using cases I–III at azimuthal radial of 213°. Shown are (a) the Ψ_{DP} profile (black) and the reconstructed Φ_{DP} using case I (blue) and case III (green). Corresponding K_{DP} profiles, with an offset of $-10°\ \text{km}^{-1}$, are shown in a similar manner. (b) As in (a), but using cases II (red) and III (green) and showing δ_{hv} instead of K_{DP}. (c) Profiles of z (black), Z^t (gray), and Z (green). (d) As in (c), but for Z_{DR}.

peaks (both of approximately $10°\ \text{km}^{-1}$) from case III correspond to fast increments of Ψ_{DP} located downrange in convective areas. Observe that the Ψ_{DP} profile includes a δ_{hv} "bump" in the range 2–4 km. To analyze the δ_{hv} contamination aspect of K_{DP}, Φ_{DP} from cases II and III are shown in Fig. 4b as well as their corresponding δ_{hv} profiles shifted by $-10°$. This δ_{hv} bump of 2-km length does not show an impact on Φ_{DP} (case II) because its length is smaller than $L_{\text{min}} = 3$ km. Also, Ψ_{DP} values outside the bump are similar and therefore most $\Delta\Psi_{\text{DP}}$ samples have values near 0°. In summary, K_{DP} estimation is not affected by this δ_{hv} bump in both cases, II and III. Note that in the range 7–11 km, Ψ_{DP} increases rapidly, which probably means that raindrops of moderate to large size are present and thus significant δ_{hv} values are expected. However, both Φ_{DP} profiles are similar. This similarity may be due to δ_{hv} values hardly varying in this range and thus $\Delta\delta_{\text{hv}}$ samples do not impact $\Delta\Psi_{\text{DP}}$ samples. Such a feature can be seen in δ_{hv} (case III), where it shows a slight spatial variability. Further, the estimation of δ_{hv} depends on Φ_{DP} estimation, which can include accumulated K_{DP} errors (e.g., toward the end of the range). A rigorous estimation and analysis of δ_{hv} are beyond the scope of this work; the focus here is on K_{DP} estimation.

Figure 4c shows attenuated z, corrected Z^t, and corrected Z profiles—the last profile being associated with case III. The correction of z is evident toward the convective range 7–11 km, where PIA reaches 15 dB at 11 km. Note that the Z^t profile shows values slightly larger than those of the Z profile because of unfiltered δ_{hv}. In a similar manner, the correction of the z_{dr} profile is shown in Fig. 4d, where PIA_{DP} equals 2.3 dB at 11 km. Note that the δ_{hv} and Z_{DR} profiles show a correlated behavior as expected from the δ_{hv}–Z_{DR} relation.

2) FOR A FULL PPI

The results from applying the K_{DP} approach, specified by case III, to all radials of Fig. 3 are shown in Fig. 5. The field of Z is plotted in Fig. 5a and the field of L, selected from the interval [3; 5] km, in Fig. 5b. The spatial variability of L exhibits an adaptive performance with the purpose of minimizing σ_K. The K_{DP} and Φ_{DP} fields are shown in Figs. 5c and 5d, respectively. It can be seen that the K_{DP} field maintains the structure and resolution of the storm illustrated by the Z field, whereas the Φ_{DP} field displays the propagation phase component of the Ψ_{DP} field depicted in Fig. 3c. Note that the K_{DP} field presents some gaps in

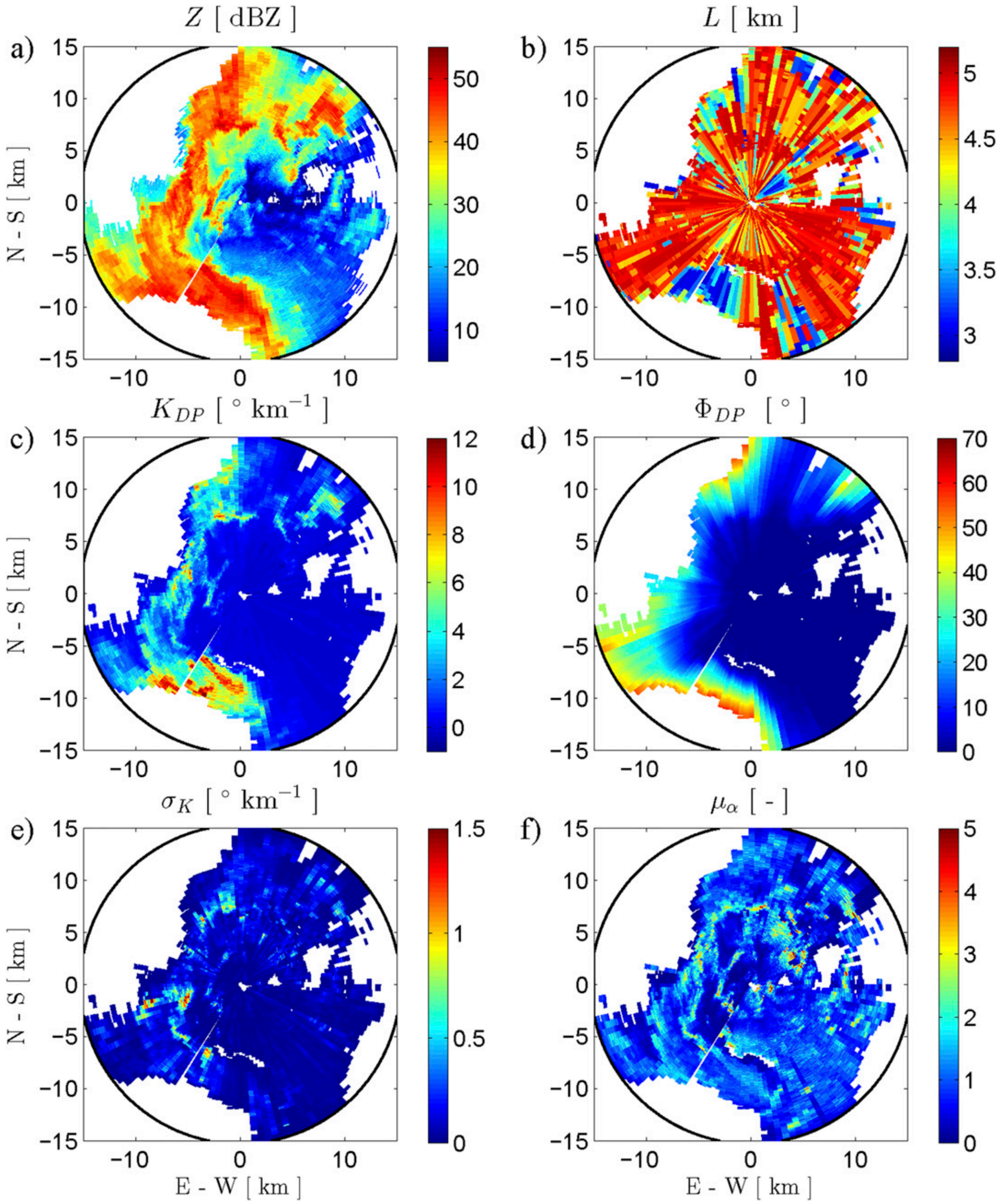

FIG. 5. PPI fields from estimating K_{DP} using case III: (a) attenuation-corrected Z, (b) selected L, (c) estimated K_{DP}, (d) reconstructed Φ_{DP}, (e) actual σ_K, and (f) actual μ_α.

areas of measured Z (e.g., at approximately 8 km south from IDRA). In these areas, M is equal to 0, which means that for any bounded value of L, none of the $(\mathrm{n}+1)$–$\Delta\Psi_{\mathrm{DP}}$ samples satisfies Eq. (5). Such an issue could be avoided if, for instance, K_{DP} is estimated using case II instead of case III or interpolation algorithms are used. Figure 5e shows the actual σ_K, whose arithmetic mean is equal to 0.1° km^{-1}. However, values as high as 1° km^{-1} are visible near convective edges. This increase in σ_K is partly due to a reduced number of $\Delta\Psi_{\mathrm{DP}}$ samples that satisfy Eq. (5). The actual μ_α are represented in Fig. 5f, whose values are mostly between 0 and 5. Thus, setting theoretical μ_α equal to 3 in this convective storm is a reasonable predefinition. The field of μ_α also shows an adaptive characteristic of the K_{DP} approach as it handles the spatial variability of Ψ_{DP}. In a similar manner, K_{DP} is estimated using cases I and II.

To study the impact of unfiltered δ_{hv} on the standard deviation of K_{DP}, actual σ_K resulting from cases II and III over all radials is displayed in Fig. 6 as a function of its corresponding number of paths M, with $M > 1$. Because of the large number of σ_K and M samples, they are plotted as 2D histograms for better visualization. Note that the σ_K–M histogram from case II shows a very small dependence on M as opposed to Eq. (11). This holds for values of M up to 167 (i.e., the nearest integer less than $L_{\max}/\Delta r + 1$). Such behavior occurs because the $\Delta\Psi_{\mathrm{DP}}$ filter condition is not applied in case II and thereafter adjacent paths are employed to obtain $\Delta\Psi_{\mathrm{DP}}$ samples, which leads to an increased correlation coefficient between these samples. In a hypothetical situation with a correlation coefficient equal to 1, theoretical σ_K is no longer a function of M [see Eq. (A2) in appendix A]. In addition to these adjacent samples, unfiltered $\Delta\delta_{\mathrm{hv}}$, and thereby δ_{hv}, compromises the estimation of K_{DP} and increases the variability of actual σ_K. In contrast, the 2D histogram from case III shows a dependence on M because σ_K decreases when M increases as expressed by the theoretical σ_K in Eq. (11). Two theoretical σ_K curves, for the same range resolution of IDRA, are also plotted in Fig. 6 to compare theoretical σ_K with actual σ_K from case III. The upper curve is set with $L = 3\,\mathrm{km}$ (i.e., $L_{\min}$) and $\mu_\alpha = 5$ and the lower curve with $L = 5\,\mathrm{km}$ (i.e., $L_{\max}$) and $\mu_\alpha = 0.5$, assuming the same theoretical values for σ_P and σ_ε as given in section 3e. For a fair comparison between actual σ_K near 0° km^{-1} and the lower σ_K curve, only actual σ_K values slightly larger than 0° km^{-1}—for example, ≥0.05° km^{-1}—are considered. In this comparison, 91% of the σ_K–M scatters are in between both curves, while only 2% are located above the upper curve.

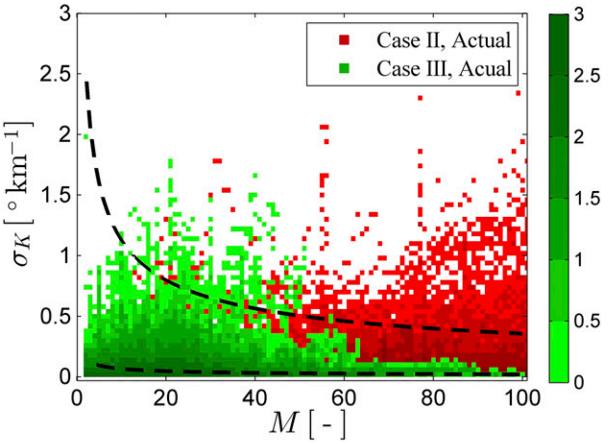

FIG. 6. 2D histograms of the actual σ_K and number of paths M resulting from case II (red) and case III (green). Theoretical σ_K curves, at $\Delta r = 0.03\,\mathrm{km}$, are indicated (dashed black), where the upper curve corresponds to $L = 3\,\mathrm{km}$ and $\mu_\alpha = 5$ and the lower curve to $L = 5\,\mathrm{km}$ and $\mu_\alpha = 0.5$. Frequency of occurrence is given in logarithm scale and applies to all subsequent histograms.

3) Z–K_{DP} RELATION

Another manner to study the downscaling and δ_{hv} contamination aspects of the K_{DP} approach is by examining the consistency between Z and K_{DP} (Park et al. 2005b). For this purpose, Fig. 7a compares the Z–K_{DP} histograms from cases I–III. In case I K_{DP} is estimated at coarse resolution and its values are smaller than 8° km^{-1}, while in cases II and III K_{DP} is estimated at Δr scales and K_{DP} values can be as high as 12° km^{-1}. However, in case II the 2D histogram shows multiple negative outliers because of unfiltered δ_{hv}, resulting in underestimated and overestimated K_{DP} values. Among these three cases, case III provides the best consistency because of the application of the $\Delta\Psi_{\mathrm{DP}}$ filter condition and $\Delta\Psi_{\mathrm{DP}}$ downscaling specified by the proposed K_{DP} approach.

For evaluation purposes, Fig. 7b shows the Z–K_{DP} histogram from case III, the Z–K_{DP} scatterplot using scattering simulation from section 2b, and its theoretical fit Z–K_{DP} relation given by $K_{\mathrm{DP}} = 8.7 \times 10^{(0.69Z/10)-4}$. Note that simulated Z values were shifted by $-8\,\mathrm{dB}$ in order to match those from case III, which could be due to incorrect attenuation correction and/or bias associated with PBB and miscalibration. In contrast, the K_{DP} axis shows a noticeable agreement between simulation and estimation. As a first step to analyze the discrepancy in the Z axis, a similar histogram is shown but with attenuated z instead of corrected Z, keeping estimated K_{DP}. From both plots it is clear that attenuation is not the major reason for this inconsistency but rather PBB and miscalibration.

d. K_{DP} *in solid or mixed precipitation*

As part of the presented analysis, K_{DP} estimation at X-band frequency over areas of solid and melting hydrometeors, such as graupel, hail, and snow, are shortly discussed. Because the shape and orientation response of particles are strongly related to their dielectric response, polarimetric signatures of solid hydrometeors is reduced because their dielectric constant factor is 20% or less that of raindrops. For example, Dolan and Rutledge (2009) and Snyder et al. (2010) simulated K_{DP} values at X band for solid and melting particles, showing a limited range of −1 to 1 (° km^{-1}) except for melting graupel, which can be between −2 to 7 (° km^{-1}). In addition, values of δ_{hv} from solid hydrometeors are small except for large nonspherical hail or melting hail, in which δ_{hv} can be in the order of 4°–7° (Trömel et al. 2013). Moreover, Schneebeli et al. (2014) calculated K_{DP} in snow using a Kalman filter–based approach and

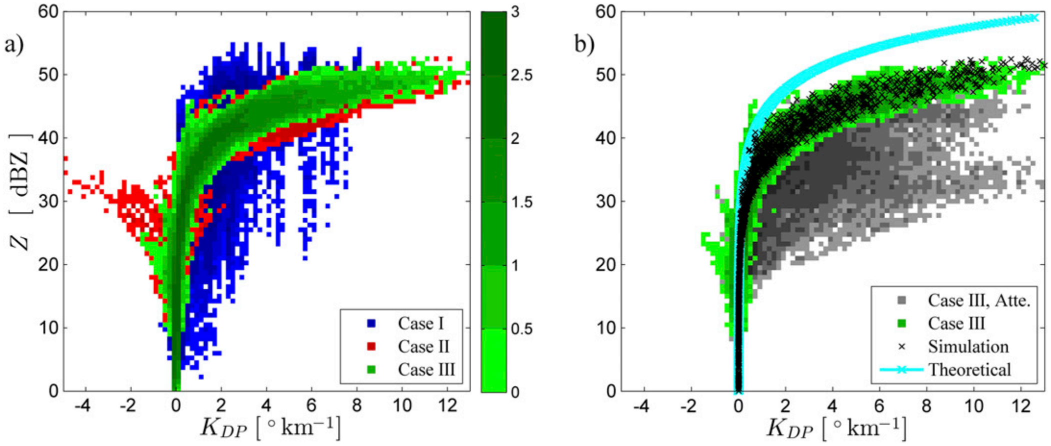

FIG. 7. (a) Histograms of Z–K_{DP} resulting from cases I (blue), II (red), and III (green) are compared. (b) As in (a), but only for case III, where the Z axis before (gray) and after (green) attenuation correction is shown. In addition, a simulated Z–K_{DP} scatterplot (1500 cross symbols) and its theoretical fit (cyan). Simulated Z values are shifted by −8 dB.

found similar results when K_{DP} is estimated by the conventional technique. In this context the spatial variability of K_{DP} in nonrain regions may be less significant than in rain regions. Thus, the conventional approach or an autoregression-based model can be considered to complement K_{DP} estimates in nonrain regions as demonstrated by Lim et al. (2013). Alternately, the adaptive high-resolution approach can be also used by setting $\hat{w}^{(j)}$ equal to $\Delta r L^{-1}$ and M equal to $n + 1$, which is similar to case I but without the $\Delta\Psi_{\mathrm{DP}}$ filter condition, at expenses of low-resolution and possibly δ_{hv} infiltration. In this scenario the theoretical σ_K is simplified to $1.5\sqrt{2\Delta r}\,L^{-1.5}$ assuming $\sigma_P = 3°$, $\mu_\alpha = 1$, and $M = n$. For instance, for Δr values of 0.03, 0.25, and 1 km, L can be set to 3, 6, and 9 km, respectively, in order to obtain a theoretical σ_K equal to 0.07° km^{-1}. However, further research is required to test the suggested alternative.

5. Assessment of the adaptive high-resolution approach

In this section the performance of the proposed K_{DP} approach specified by case III is compared with the conventional and high-resolution (HR) techniques. For this purpose, four storm events (E1–E4) observed by IDRA are described in Table 2. Although only observations of E3 at 1950 UTC were shown in section 4, the other events also display patterns related to attenuation, PBB, and miscalibration. In the conventional technique, the filter is designed using a 36th-order filter with $r_c = 1$ km and $\tau = 1.5\sigma_P$. More details on the filter design are included in appendix B.

a. During 1 min

The corresponding times for E1–E4 are 2151, 2225, 1950, and 0550 UTC, respectively. The Z–K_{DP} histograms resulting from the three K_{DP} approaches applied to each 1-min event (i.e., one PPI) are shown in Fig. 8. The Z–K_{DP} scatters from the conventional technique are significantly spread because K_{DP} is estimated at coarse resolution and δ_{hv} is not properly filtered, which leads to negative and positive K_{DP} bias. In contrast, results from the HR method show more condensed relations. However, for Z values smaller than approximately 40 dBZ, multiple outliers are noticeable. Those outliers are substantially eliminated by the adaptive HR approach, which exhibits an enhanced consistency for weak and strong Z. To quantify the consistency of the results, the correlation coefficient between Z and K_{DP}, $\rho_{Z,K}$, obtained from each approach is given by the second, third, and fourth columns of Table 3. From this quantification, the adaptive HR approach outperforms the other two techniques. For reference purposes, the $\rho_{Z,K}$ from the simulated Z–K_{DP} shown in Fig. 7b was also estimated and is equal to 0.75, which is similar to those resulted from the adaptive HR technique. Note that $\rho_{Z,K}$ values resulting from simulation or observations can change according to the range of Z and K_{DP} values because the theoretical Z–K_{DP} relation is nonlinear and thereby $\rho_{Z,K}$ may be used as a relative quantity.

The results of Z and K_{DP} from the conventional and adaptive HR methods, presented in Fig. 8, show a similar discrepancy in the Z axis as indicated in Fig. 7b. Although the degree of discrepancy is not the same in all events, the Z values reached by the conventional

TABLE 2. Description of four storm events observed by IDRA with coverage of 15.3 km and $\Delta r = 0.03$ km.

Events	Date	Period (UTC)	Storm type
E1	10 May 2011	2100–2300	Single cells,[a] light and moderate rain
E2	28 Jun 2011	2200–0000	A cluster of multicells (moderate rain) followed by a widespread area of light rain
E3	10 Sep 2011	1940–2140	A cell larger than 100 km^2 followed by single cells, moderate and heavy rain
E4	7 Oct 2011	0420–0620	Cells of irregular shapes, light and moderate rain

[a] Area of a cell is found in the range 10–100 km^2 with Z larger than 30 dBZ. Similar cell characteristics are defined by Johnson et al. (1998).

technique are in the same order as those from the adaptive HR approach. This indicates that Z is most likely biased and that the estimation of K_{DP} by the adaptive HR approach may not be affected by attenuation and biases associated with PBB and/or miscalibration.

A second manner to quantify the performance of the adaptive HR approach is by comparing its actual σ_K and σ_K^n, which were introduced as quality measures in section 3d, with the HR method for each event. The mean values of the σ_K field ($\overline{\sigma_K}$) and σ_K^n field ($\overline{\sigma_K^n}$) resulting from these techniques are given in Table 3. For the calculation of $\overline{\sigma_K^n}$, only gates with $|K_{\mathrm{DP}}| \geq 1^\circ\ \mathrm{km}^{-1}$ are considered. Note that $\overline{\sigma_K}$ from the adaptive HR approach is, on average, one-tenth of the HR method. In addition, $\overline{\sigma_K^n}$ results from the adaptive HR approach are smaller than a reasonable error of 20%, while those from the HR method are much larger than 20%. Another quality measure, also given in section 3d, is σ_α^n, which measures the percentage error of the actual μ_α estimated by the adaptive HR approach. The mean of the σ_α^n field ($\overline{\sigma_\alpha^n}$) for each event is found reasonably small as indicated in Table 3. Finally, in terms of computational time required by both techniques, the adaptive HR approach needs, on average, one-third of the time required by the HR method, which is on the order of a few minutes for 1 min of data, while for the conventional technique it is on the order of seconds.

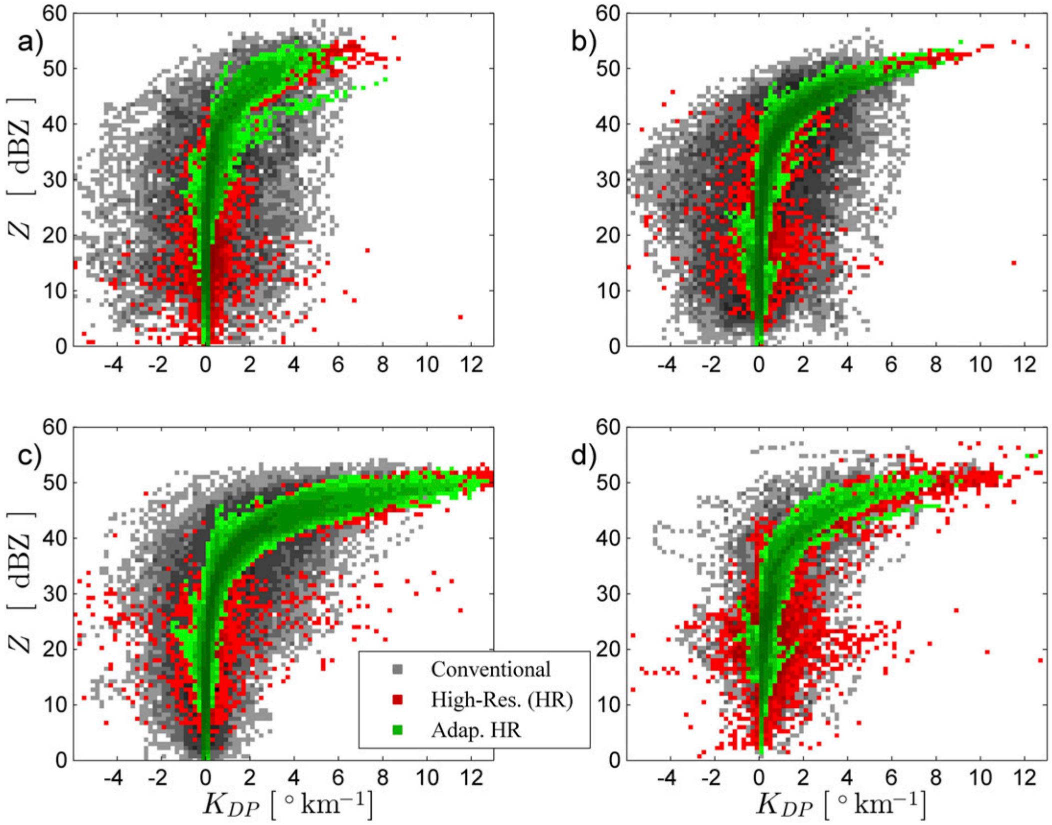

FIG. 8. (a) Histograms of Z–K_{DP} for event E1. Conventional (gray), HR (red), and adaptive HR (green) approaches. (b)–(d) As in (a), but for E2–E4, respectively.

TABLE 3. Comparison of the three K_{DP} approaches—conventional (conv), HR, and adaptive HR (adap HR)—for the four storm events quantified by $\rho_{Z,K}$, $\overline{\sigma_K}$, $\overline{\sigma_K^n}$, and $\overline{\sigma_\alpha^n}$.

	$\rho_{Z,K}$ (-)			$\overline{\sigma_K}$ (° km^{-1})		$\overline{\sigma_K^n}$ (%)		$\overline{\sigma_\alpha^n}$ (%)
Event	Conv	HR	Adap HR	HR	Adap HR	HR	Adap HR	Adap HR
E1	0.38	0.61	0.72	1.12	0.09	85	16	11
E2	0.48	0.70	0.74	0.93	0.09	50	9	13
E3	0.66	0.73	0.75	0.83	0.10	42	7	16
E4	0.53	0.67	0.75	1.22	0.06	83	6	10

b. During 2 h

Next, the three K_{DP} techniques are compared and evaluated using the same quality measures $\rho_{Z,K}$, $\overline{\sigma_K}$, $\overline{\sigma_K^n}$, and $\overline{\sigma_\alpha^n}$ and storm events E1–E4 but during 2-h periods as illustrated in Figs. 9–12, respectively. In general, it can be observed that the adaptive HR approach outperforms the other two methods, although the performance of each technique varies according to the storm scenario. For example, the conventional technique can lead to reasonable results when a storm consists of a large area of heavy rain because Ψ_{DP} profiles carry sufficient data samples with high SNR levels, reducing the impact from Ψ_{DP} outliers. In the HR method, acceptable results can be obtained in a scenario given by a large cell or a cluster of multiple cells with moderate to heavy rain because it allows for consideration of multiple $\Delta\Psi_{DP}$ samples over extended paths, which reduces the impact of small and sometimes negative $\Delta\Psi_{DP}$ values. In addition, this scenario may reduce the sensitivity of the downscaling weight $w(i)$ to noisy measurements of Z and Z_{DR}. In contrast, the adaptive HR approach yields reliable results even when storm cells cover relatively small areas with light rain because $\Delta\Psi_{DP}$ samples are adaptively selected over paths with lengths determined from a predefined interval so that a theoretical value of σ_K is minimized. Moreover, uncertainties associated with the SC relation are reduced as a result of the improved formulation of $w(i)$ in this method. In case a storm cell becomes significantly small, such that the extents of Ψ_{DP} profiles are on the order of L_{min}, estimates of K_{DP} by the adaptive HR approach are not possible; this feature could be beneficial because accurate estimation of K_{DP} from limited data samples is rarely achieved.

The resulting time series of $\rho_{Z,K}$ for event E3 indicate that during the first hour, the three K_{DP} approaches performed in a similar manner because K_{DP} estimates were obtained from a large cell with heavy rain in which the conventional and HR methods perform at their best. During the second hour, small cells with moderate rain were observed, leading to decreased performance of the conventional and HR methods. In event E2, during 2220–2300 UTC, the HR and adaptive HR approaches provided similar results and performed better than the conventional technique because this period was associated with a cluster of cells with moderate rain. After this period the adaptive HR approach maintained a satisfactory performance, while the performance of the conventional and HR methods decreased because values of K_{DP} were estimated from light rain. For events E1 and E4, $\rho_{Z,K}$ time series obtained from the conventional and HR techniques are similar but smaller than those from the adaptive HR approach because in these events single cells with irregular shapes and light rain

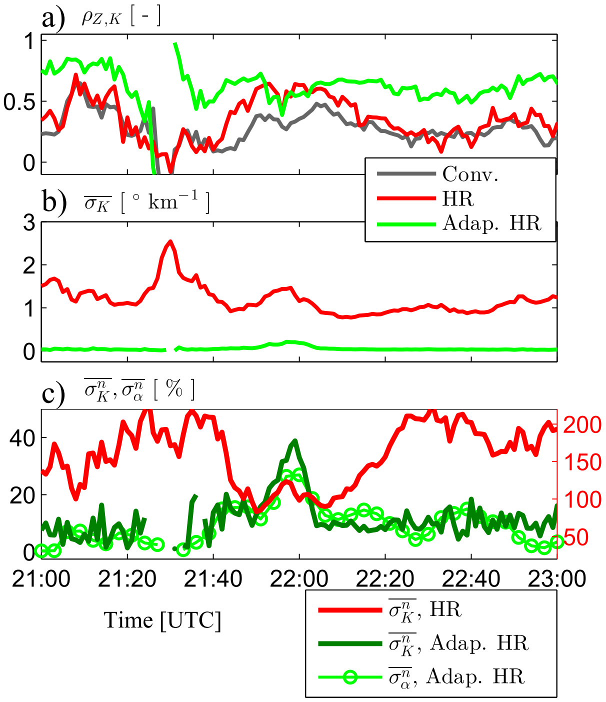

FIG. 9. Time series of quality measures from the three K_{DP} approaches for event E1. (a) Correlation coefficients from the conventional (gray), HR (red), and adaptive HR (green) techniques. (b) Mean values $\overline{\sigma_K}$ from the HR (red) and adaptive HR (green) approaches. (c) The $\overline{\sigma_K^n}$ from the HR (red, right y axis) and adaptive HR (green, left y axis) approaches. Also $\overline{\sigma_\alpha^n}$ from the adaptive HR approach (green line with circles, left y axis).

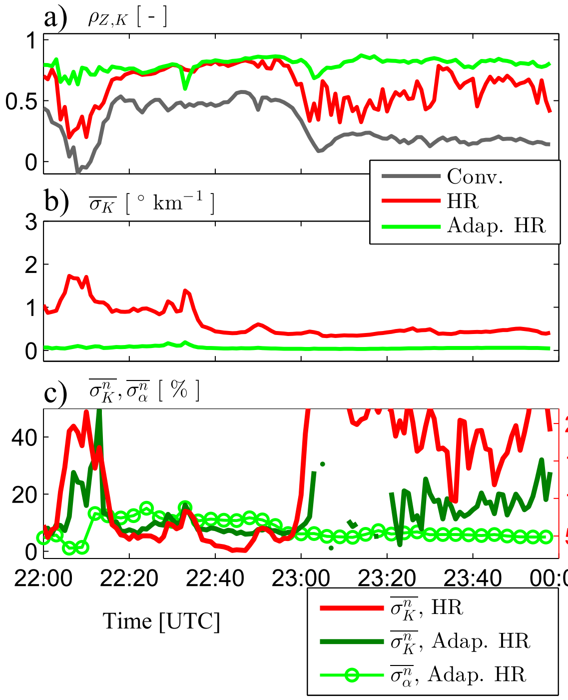

FIG. 10. As in Fig. 9, but for event E2.

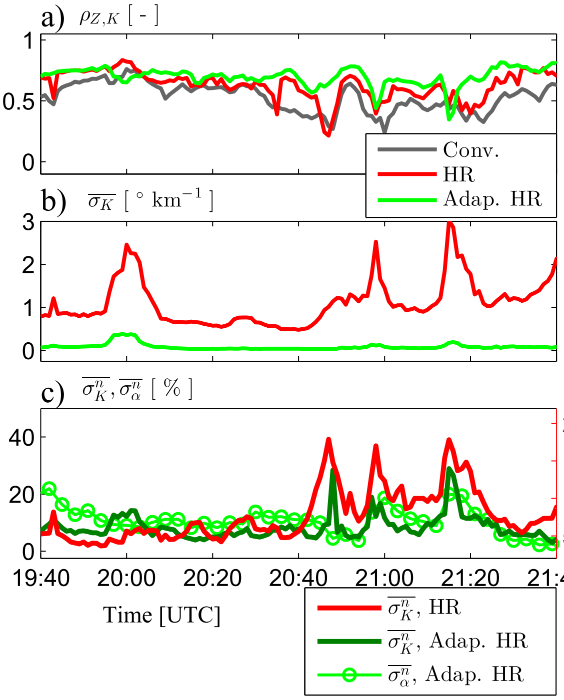

FIG. 11. As in Fig. 9, but for event E3.

were observed. Although $\rho_{Z,K}$ time series from the three K_{DP} techniques can show similar results for a given storm scenario, Z–K_{DP} relations might include multiple scatters as illustrated in Fig. 8, especially for weak Z values. As a result, the adaptive HR approach provides the best Z–K_{DP} consistency for storm scenarios with different cell sizes and rain amounts.

Time series of $\overline{\sigma_K}$ from the HR and adaptive HR techniques for the four events exhibited values between 1 and 3 and near 0 (° km^{-1}). However, the results from the HR technique for event E2 showed values smaller than 1° km^{-1} because of a widespread area of rain with low variability on Z, Z_{DR}, and Ψ_{DP} fields. Nonetheless, its performance measured by $\rho_{Z,K}$ remains below the adaptive HR approach. This shows a persistent accuracy in estimating K_{DP} by the adaptive HR approach. Furthermore, time series of $\overline{\sigma_K^n}$ and $\overline{\sigma_\alpha^n}$ resulting from the adaptive HR approach depicted, in all events, consistent percentage errors smaller than 20%. However, for events E1 (around 2200 UTC) and E3 (during some periods after 2040 UTC), the percentage errors increased because of inaccurate measurements of Z and Z_{DR} resulting from storm cells with heavy rain located adjacent to or on top of the radar, leading to power saturation in the receiver. This is an example of how $\sigma_K^n(i)$ or $\overline{\sigma_K^n}$ and $\sigma_\alpha^n(i)$ or $\overline{\sigma_\alpha^n}$ can be used to identify areas where K_{DP} estimates could be compromised. Another example of large $\overline{\sigma_K^n}$ can be seen in E2 around 2210 UTC, when $\overline{\sigma_K^n}$ values are as high as 40% because of small areas of light rain with a reduced number of $\Delta\Psi_{\mathrm{DP}}$ samples, affecting the accuracy of K_{DP} estimates. The discontinuity seen between 2300 and 2320 UTC is due to the constraint $|K_{\mathrm{DP}}| \geq 1°\ \mathrm{km}^{-1}$. A similar discontinuity is observed in event E1 around 2130 UTC. During the same event, a decreasing and discontinued behavior of $\rho_{Z,K}$ is observed in the period 2120–2140 UTC. Such behavior is associated with a progressive reduction of storm cells in intensity and size, which led to light rain echoes with areas smaller than 5 km^2 where the extents of Ψ_{DP} profiles are not sufficient for the estimation of K_{DP}. This means that K_{DP} cannot be estimated over a Ψ_{DP} segment whose length is on the order of or smaller than $L_{\min}$. For the case of the HR method, the time series of $\overline{\sigma_K^n}$ indicated a limited performance, as $\overline{\sigma_K^n}$ values are mostly larger than 50%.

6. Conclusions

Polarimetric studies have continuously focused on the estimation of K_{DP} because of its capability to overcome power attenuation and radar miscalibration. However, accurate estimation of K_{DP} at scales of the range resolution is challenging because K_{DP} requires significant spatial smoothing because of noisy Ψ_{DP} profiles, for example, in light rain. This problem is intensified at short wavelengths when Ψ_{DP} profiles include δ_{hv} components,

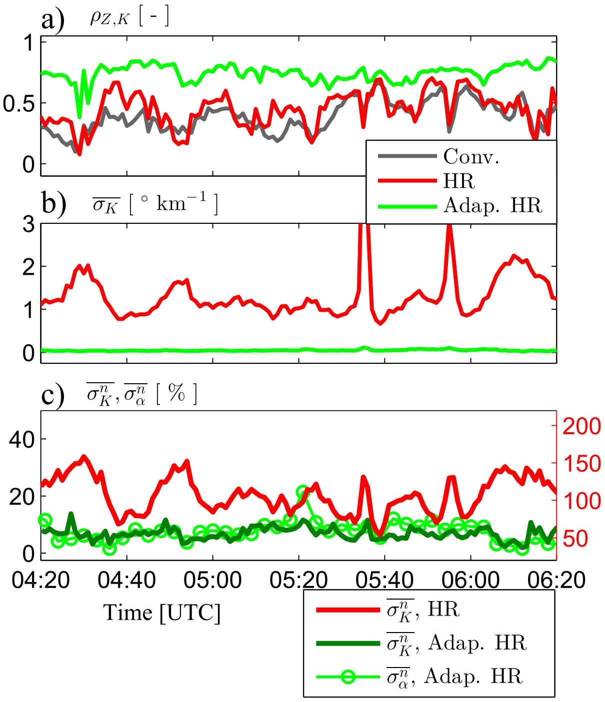

FIG. 12. As in Fig. 9, but for event E4.

for example, in moderate and heavy rain. In this work an adaptive HR approach has been presented to address these problems. The standard deviation of the proposed K_{DP} estimator has been derived and formulated in order to provide a pathlength interval that could lead to K_{DP} estimates with reduced error. This formulation takes into account the spatial variability of the storm and the radar range resolution.

A storm event observed by a polarimetric X-band weather radar during 1 min was used to analyze and test the performance of the K_{DP} estimator. Results showed that the estimated K_{DP} field kept the structure of the attenuation-corrected Z field without significant spatial distortion and that its estimation was associated with reduced errors indicated by the actual standard deviation (i.e., the σ_K field). The consistency between Z and K_{DP} showed that negative values of K_{DP}, associated with weak Z, can be reduced and that high K_{DP} values, associated with strong Z, can be obtained. To assess the performance of the adaptive HR approach to obtain accurate K_{DP} at range resolution scales, four storm events observed by the same radar but during 2-h periods were considered and the K_{DP} results were compared with the conventional and HR techniques. In general, the proposed approach was able to provide a correlation coefficient between Z and K_{DP} higher than the other two methods. In terms of standard deviations, the adaptive HR approach showed significant improvements compared to the HR technique. The actual μ_α field, introduced by the adaptive HR approach, was associated with reduced uncertainty as indicated by the $\overline{\sigma_\alpha^n}$ results. However, it was observed that the adaptive HR approach is able only to estimate K_{DP} over Ψ_{DP} segments larger than $L_{\min}$ and where the number of $\Delta\Psi_{\mathrm{DP}}$ samples is larger than 0.

Although the adaptive HR approach considers measurements of Z and Z_{DR} and constant coefficients related to the SC relation and attenuation correction in rain, the results of this method did not highlight issues related to radar miscalibration, radial patterns in Z_{DR} as a result of PBB, power attenuation, and variability on DSD and drop shape. Consequently, the adaptive HR approach, which uses the correlation between δ_{hv} and Z_{DR} and the SC relation, is able to filter δ_{hv} and maintain the spatial variability of Ψ_{DP}. Therefore, accurate K_{DP} profiles at high spatial resolution in light and heavy rain are achieved. However, if measurements of Z and Z_{DR} are associated with low SNR levels or are affected by offsets that fluctuate along a given radial, then it is expected that the accuracy of the downscaling weights and thereby K_{DP} estimates will be reduced. In general, quality control variables σ_K^n or σ_α^n, which are associated with percentage errors larger than, for example, 20%, might lead to inaccurate K_{DP} estimates.

To achieve the ambitions of implementing the proposed K_{DP} algorithm for real-time operation, further studies are required. This effort includes estimating and updating the coefficients, which are used in the attenuation correction method and in the SC principle, to operational C- and S-band frequencies and, if possible, taking into account temperature variability. Note that at S-band frequency, the $\Delta\Psi_{\mathrm{DP}}$ filter condition can be excluded from the K_{DP} algorithm because δ_{hv} is usually negligible. Moreover, an automatic algorithm might be needed to classify areas of rain, nonrain, and nonhydrometeors. For solid or mixed rain areas, either the SC ratio should be set to 1, so that K_{DP} is given at expenses of coarse spatial resolution, or another K_{DP} algorithm should be employed. Furthermore, $[L_{\min}; L_{\max}]$ should be selected according to values of Δr and to predefined values of μ_α and σ_P; the latter two can be set as a function of the rain scenario (e.g., 4 and 3° for convective and 1 and 2° for stratiform rain). Last, it is recommended to evaluate the proposed approach at longer ranges, where attenuation and nonuniform beamfilling affect the Z and Z_{DR} measurements, and in scenarios where PBB is associated with complex terrain features.

A reliable K_{DP} is one of the most powerful observables from polarimetric weather radars. The adaptive HR approach may prove to be key in addressing the dilemma between the spatial resolution and the accuracy of K_{DP}

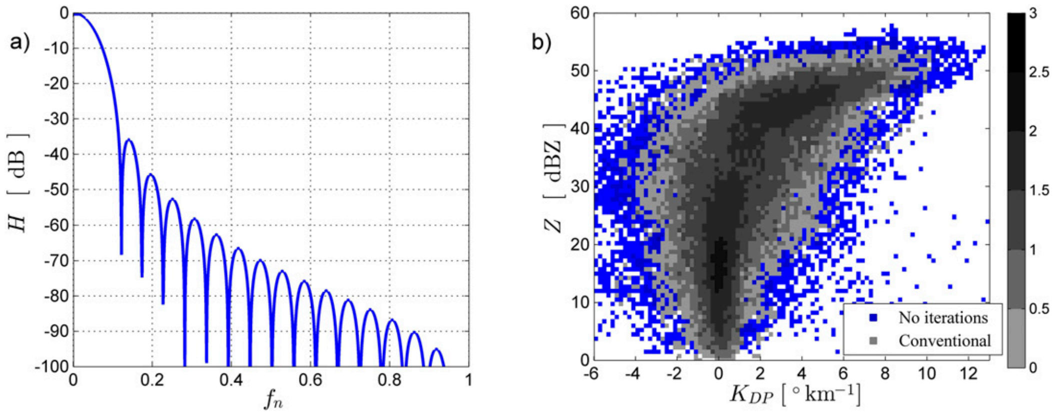

FIG. B1. (a) Magnitude response of a FIR low-pass filter specified by $r_c = 1$ km, $\Delta r = 0.03$ km, filter order of 36, and Hann window. (b) Histograms of Z–$K_{\rm DP}$ from the first step (blue) and both steps (gray) of the conventional approach.

in rain. Moreover, the formulation of the theoretical σ_K and the capability of calculating the uncertainty of $K_{\rm DP}$ estimates gate by gate allow for reducing and controlling the errors in the estimation of $K_{\rm DP}$. Even though this approach still needs to be tested in operational environments, urban hydrology and weather forecast communities may benefit from the proposed approach in terms of spatial resolution, accuracy, and quality control of $K_{\rm DP}$ estimates, which can lead to significant improvements in $K_{\rm DP}$ -based products.

Acknowledgments. We are grateful to 4TU Centre for Research Data for its support in keeping IDRA data an open access dataset (Russchenberg et al. 2010). The authors extend their deep gratitude to the anonymous reviewers for their constructive reviews, which helped to improve this paper. This work was supported by RainGain through INTERREG IVB NWE Programme.

APPENDIX A

Standard Deviation of the $K_{\rm DP}$ Estimator

For the purpose of deriving σ_K, the weight in Eq. (8) is expressed as $\hat{w}^{(j)} = \hat{\alpha}^{(j)}\Delta r/L$ and therefore the $K_{\rm DP}$ estimator given by Eq. (9) is rewritten as

$$K_{\rm DP}=\frac{1}{2L}\left[\frac{1}{M}\sum_{j=1}^{M}\Delta\Psi_{DP}^{(j)}\alpha^{(j)}\right];\quad \text{with}\quad j=1,2,\ldots M. \tag{A1}$$

Note that this expression includes the pathlength L and omits the index i for simplicity. Both $\Delta\Psi_{\rm DP}^{(j)}$ and $\alpha^{(j)}$ are considered to be independent random variables (rvs) and hence their product is also an rv and denoted by $\kappa^{(j)}$ with $j = 1, 2, \ldots M$. Assume that $\kappa^{(1)}, \kappa^{(2)}, \ldots, \kappa^{(M)}$ have the same variance σ_κ^2 and that the pair $[\kappa^{(j)}, \kappa^{(m)}]$, with $j \neq m$, has a constant covariance γ_κ. Using the variance property of the sum of correlated rvs and the relation $\gamma_\kappa = \sigma_\kappa^2\rho_\kappa$, where ρ_κ is the correlation coefficient, the variance of the $K_{\rm DP}$ estimator σ_K^2 is expressed as

$$\sigma_K^2=\frac{1}{(2ML)^2}M\sigma_\kappa^2[1+(M-1)\rho_\kappa]. \tag{A2}$$

If the term σ_κ^2 is rewritten using $\Delta\Psi_{\rm DP}^{(j)}$ and $\alpha^{(j)}$, we obtain

$$\sigma_K^2=\frac{1}{(2L\sqrt{M})^2}[\mu_\alpha^2\sigma_\Delta^2+\sigma_\alpha^2(\mu_\Delta^2+\sigma_\Delta^2)][1+(M-1)\rho_\kappa], \tag{A3}$$

where μ_α and μ_Δ represent the mean of $\alpha^{(j)}$ and $\Delta\Psi_{\rm DP}^{(j)}$, respectively. Similarly, σ_α^2 and σ_Δ^2 indicate their variance. Equation (A3) can be reduced if ρ_κ and σ_α^2 are assumed to be significantly small. In consequence, Eq. (A3) is simplified to

$$\sigma_K^2=\frac{\mu_\alpha^2\sigma_\Delta^2}{(2L\sqrt{M})^2}. \tag{A4}$$

To include residuals from the $\Delta\Psi_{\rm DP}$ filter condition (i.e., neglecting $\Delta\delta_{\rm hv}$), the difference in differential phase is represented by the sum of two uncorrelated rvs: $\Delta\Psi_{\rm DP}^{(j)} + \varepsilon_\delta^{(j)}$, where $\varepsilon_\delta^{(j)}$ has a mean and variance equal to 0° and σ_ε^2, respectively. Thus, Eq. (A4) is rewritten as

$$\sigma_K^2=\frac{\mu_\alpha^2(\sigma_\Delta^2+\sigma_\varepsilon^2)}{(2L\sqrt{M})^2}. \tag{A5}$$

For a given path $\overline{ab}$, $\Delta\Psi_{\rm DP}^{(j)}$ is expressed as $\Psi_{\rm DP}(b) - \Psi_{\rm DP}(a)$, which is the difference between two rvs. If both rvs have the same variance σ_P^2, then the variance of $\Delta\Psi_{\rm DP}^{(j)}$ is given by $\sigma_\Delta^2 = 2\sigma_P^2$. As a result, a theoretical σ_K for the K_{DP} estimator is defined as

$$\sigma_K = \frac{\mu_\alpha}{L}\sqrt{\frac{2\sigma_P^2 + \sigma_\varepsilon^2}{4M}}. \qquad \text{(A6)}$$

APPENDIX B

Filter Design to Estimate K_{DP} by the Conventional Technique

A finite impulse response (FIR) filter type is selected for designing the light filter (first step). The filter order is set to 36, while the required r_c is set to 1 km. In addition, a Hann window function is included to obtain a magnitude response H (dB) with small sidelobes. The response H is shown in Fig. B1(a) as a function of the normalized range scale $f_n = \Delta r/r_s$, where $r_s \geq \Delta r$ and r_s in km. Note that H reaches approximately −40 dB at $f_n = 0.1$. This means that the light filter is designed such that spatial variations at range scales smaller than 0.3 km are suppressed. Next, this filter is iterated several times (second step) by setting τ equal to $1.5\sigma_p$. The storm event E3 at 1950 UTC is used for demonstration purposes. The Z–K_{DP} histograms from the first and second steps are shown in Fig. B1(b). Observe that the iterative step eliminates several outliers without excessively smoothing K_{DP}.

REFERENCES

Adachi, A., T. Kobayashi, and H. Yamauchi, 2015: Estimation of raindrop size distribution and rainfall rate from polarimetric radar measurements at attenuating frequency based on the self-consistency principle. *J. Meteor. Soc. Japan*, **93**, 359–388, https://doi.org/10.2151/jmsj.2015-020.

Beck, J., and O. Bousquet, 2013: Using gap-filler radars in mountainous regions to complement a national radar network: Improvements in multiple-Doppler wind syntheses. *J. Appl. Meteor. Climatol.*, **52**, 1836–1850, https://doi.org/10.1175/JAMC-D-12-0187.1.

Berne, A., and W. Krajewski, 2013: Radar for hydrology: Unfulfilled promise or unrecognized potential? *Adv. Water Resour.*, **51**, 357–366, https://doi.org/10.1016/j.advwatres.2012.05.005.

Bringi, V. N., and V. Chandrasekar, 2001: *Polarimetric Doppler Weather Radar: Principles and Applications*. Cambridge University Press, 636 pp.

——, ——, N. Balakrishman, and D. Zrnić, 1990: An examination of propagation effects in rainfall on radar measurements at microwave frequencies. *J. Atmos. Oceanic Technol.*, **7**, 829–840, https://doi.org/10.1175/1520-0426(1990)007<0829:AEOPEI>2.0.CO;2.

Dolan, B., and S. A. Rutledge, 2009: A theory-based hydrometeor identification algorithm for X-band polarimetric radars. *J. Atmos. Oceanic Technol.*, **26**, 2071–2088, https://doi.org/10.1175/2009JTECHA1208.1.

Doviak, R. J., V. Bringi, A. Ryshkov, A. Zahrai, and D. Zrnić, 2000: Considerations for polarimetric upgrades to operational WSR-88D radars. *J. Atmos. Oceanic Technol.*, **17**, 257–278, https://doi.org/10.1175/1520-0426(2000)017<0257:CFPUTO>2.0.CO;2.

Ernsdorf, T., B.-R. Beckman, I. Sölch, A. Augst, M. Hagen, and T. Schubert, 2015: Application of X-band radar and lidar wind measurement at Frankfurt and Munich airports for air traffic management (ATM). *37th Conf. on Radar Meteorology*, Norman, OK, Amer. Meteor. Soc., 284, https://ams.confex.com/ams/37RADAR/webprogram/Paper276619.html.

Figueras i Ventura, J., 2009: Design of a high resolution X-band Doppler polarimetric radar. Ph.D. thesis, Delft University of Technology, 162 pp.

Giangrande, S., and A. V. Ryzhkov, 2005: Calibration of dual-polarization radar in the presence of partial beam blockage. *J. Atmos. Oceanic Technol.*, **22**, 1156–1166, https://doi.org/10.1175/JTECH1766.1.

——, R. McGraw, and L. Lei, 2013: An application of linear programming to polarimetric radar differential phase processing. *J. Atmos. Oceanic Technol.*, **30**, 1716–1729, https://doi.org/10.1175/JTECH-D-12-00147.1.

Goddard, J., J. Tan, and M. Thurai, 1994: Technique for calibration of meteorological radars using differential phase. *Electron. Lett.*, **30**, 166–167, https://doi.org/10.1049/el:19940119.

Gorgucci, E., and V. Chandrasekar, 2005: Evaluation of attenuation correction methodology for dual-polarization radars: Application to X-band systems. *J. Atmos. Oceanic Technol.*, **22**, 1195–1206, https://doi.org/10.1175/JTECH1763.1.

——, G. Scarchilli, and V. Chandrasekar, 1992: Calibration of radars using polarimetric techniques. *IEEE Trans. Geosci. Remote Sens.*, **30**, 853–858, https://doi.org/10.1109/36.175319.

——, ——, and ——, 1999: Specific differential phase estimation in the presence of nonuniform rainfall medium along the path. *J. Atmos. Oceanic Technol.*, **16**, 1690–1697, https://doi.org/10.1175/1520-0426(1999)016<1690:SDPEIT>2.0.CO;2.

Gourley, J. J., A. J. Illingworth, and P. Tabary, 2009: Absolute calibration of radar reflectivity using redundancy of the polarization observations and implied constraints on drop shapes. *J. Atmos. Oceanic Technol.*, **26**, 689–703, https://doi.org/10.1175/2008JTECHA1152.1.

Grazioli, J., M. Schneebeli, and A. Berne, 2014: Accuracy of phase-based algorithm for the estimation of the specific differential phase shift using simulated polarimetric weather radar data. *IEEE Geosci. Remote Sens. Lett.*, **11**, 763–767, https://doi.org/10.1109/LGRS.2013.2278620.

Heinselman, P. L., and S. Torres, 2011: High-temporal-resolution capabilities of the National Weather Radar Testbed Phased-Array Radar. *J. Appl. Meteor. Climatol.*, **50**, 579–593, https://doi.org/10.1175/2010JAMC2588.1.

Hu, Z., L. Liu, L. Wu, and Q. Wei, 2015: A comparison of de-noising methods for differential phase shift and associated rainfall estimation. *J. Meteor. Res.*, **29**, 315–327, https://doi.org/10.1007/s13351-015-4062-6.

Huang, 2015: The improvement to the specific differential phase estimation with the modified linear programming method. *37th Conf. on Radar Meteorology*, Norman, OK, Amer. Meteor. Soc., 13B.5, https://ams.confex.com/ams/37RADAR/webprogram/Paper275638.html.

Hubbert, J., and V. N. Bringi, 1995: An iterative filtering technique for the analysis of copolar differential phase and dual-frequency radar measurements. *J. Atmos. Oceanic Technol.*, **12**, 643–648, https://doi.org/10.1175/1520-0426(1995)012<0643:AIFTFT>2.0.CO;2.

Johnson, J. T., P. L. MacKeen, A. Witt, E. D. Mitchell, G. J. Stumpf, M. D. Eilts, and K. W. Thomas, 1998: The Storm Cell Identification and Tracking algorithm: An enhanced WSR-88D algorithm. *Wea. Forecasting*, **13**, 263–276, https://doi.org/10.1175/1520-0434(1998)013<0263:TSCIAT>2.0.CO;2.

Leijnse, H., and Coauthors, 2010: Precipitation measurement at CESAR, the Netherlands. *J. Hydrometeor.*, **11**, 1322–1329, https://doi.org/10.1175/2010JHM1245.1.

Lengfeld, K., M. Clemens, C. Merker, H. Münster, and F. Ament, 2016: A simple method for attenuation correction in local X-band radar measurements using C-band radar data. *J. Atmos. Oceanic Technol.*, **33**, 2315–2329, https://doi.org/10.1175/JTECH-D-15-0091.1.

Lim, S., R. Cifelli, V. Chandrasekar, and S. Y. Matrosov, 2013: Precipitation classification and quantification using X-band dual-polarization weather radar: Application in the Hydrometeorology Testbed. *J. Atmos. Oceanic Technol.*, **30**, 2108–2120, https://doi.org/10.1175/jtech-D-12-00123.1.

Matrosov, S. Y., K. Clark, B. Martner, and A. Tokay, 2002: X-band polarimetric radar measurements of rainfall. *J. Appl. Meteor.*, **41**, 941–952, https://doi.org/10.1175/1520-0450(2002)041<0941:XBPRMO>2.0.CO;2.

——, R. Cifelli, P. C. Kennedy, S. W. Nesbitt, S. A. Rutledge, V. N. Bringi, and B. E. Martner, 2006: A comparative study of rainfall retrievals based on specific differential phase shifts at X- and S- band radar frequencies. *J. Atmos. Oceanic Technol.*, **23**, 952–963, https://doi.org/10.1175/JTECH1887.1.

McLaughlin, D., and Coauthors, 2009: Short-wavelength technology and the potential for distributed networks of small radar systems. *Bull. Amer. Meteor. Soc.*, **90**, 1797–1817, https://doi.org/10.1175/2009BAMS2507.1.

Ochoa-Rodriguez, S., and Coauthors, 2015: Impact of spatial and temporal resolution of rainfall inputs on urban hydrodynamic modelling outputs: A multi-catchment investigation. *J. Hydrol.*, **531**, 389–407, https://doi.org/10.1016/j.jhydrol.2015.05.035.

Otto, T., and H. W. J. Russchenberg, 2011: Estimation of specific differential phase and differential backscatter phase from polarimetric weather radar measurements of rain. *IEEE Geosci. Remote Sens. Lett.*, **8**, 988–992, https://doi.org/10.1109/LGRS.2011.2145354.

Park, S.-G., V. N. Bringi, V. Chandrasekar, M. Maki, and K. Iwanami, 2005a: Correction of radar reflectivity and differential reflectivity for rain attenuation at X band. Part I: Theoretical and empirical basis. *J. Atmos. Oceanic Technol.*, **22**, 1621–1632, https://doi.org/10.1175/JTECH1803.1.

——, M. Maki, K. Iwanami, V. N. Bringi, and V. Chandrasekar, 2005b: Correction of radar reflectivity and differential reflectivity for rain attenuation at X band. Part II: Evaluation and application. *J. Atmos. Oceanic Technol.*, **22**, 1633–1655, https://doi.org/10.1175/JTECH1804.1.

Russchenberg, H., T. Otto, R. Reinoso-Rondinel, C. Unal, and J. Yin, 2010: IDRA weather radar measurements—All data. 4TU Centre for Research Data, Delft University of Technology. Subset used: IDRA Processed Data with standard range, accessed 12 October 2012, https://doi.org/10.4121/uuid:5f3bcaa2-a456-4a66-a67b-1eec928cae6d.

Ryzhkov, A. V., and D. Zrnić, 1996: Assessment of rainfall measurement that uses specific differential phase. *J. Appl. Meteor. Climatol.*, **35**, 2080–2090, https://doi.org/10.1175/1520-0450(1996)035<2080:AORMTU>2.0.CO;2.

——, S. E. Giangrande, and T. J. Schuur, 2005: Rainfall estimation with a polarimetric prototype of WSR-88D. *J. Appl. Meteor.*, **44**, 502–515, https://doi.org/10.1175/JAM2213.1.

Scarchilli, G., E. Gorgucci, V. Chandrasekar, and T. A. Seliga, 1993: Rainfall estimation using polarimetric techniques at C-band frequencies. *J. Appl. Meteor. Climatol.*, **32**, 1150–1160, https://doi.org/10.1175/1520-0450(1993)032<1150:REUPTA>2.0.CO;2.

——, ——, ——, and A. Dobaie, 1996: Self-consistency of polarization diversity measurement of rainfall. *IEEE Trans. Geosci. Remote Sens.*, **34**, 22–26, https://doi.org/10.1109/36.481887.

Schellart, A., W. Shepherd, and A. Saul, 2012: Influence of rainfall estimation error and spatial variability on sewer flow prediction at a small urban scale. *Adv. Water Resour.*, **45**, 65–75, https://doi.org/10.1016/j.advwatres.2011.10.012.

Schneebeli, M., and A. Berne, 2012: An extended Kalman filter framework for polarimetric X-band weather radar data processing. *J. Atmos. Oceanic Technol.*, **29**, 711–730, https://doi.org/10.1175/JTECH-D-10-05053.1.

——, J. Grazioli, and A. Berne, 2014: Improved estimation of the specific differential phase shift using a compilation of Kalman filter ensembles. *IEEE Trans. Geosci. Remote Sens.*, **52**, 5137–5149, https://doi.org/10.1109/TGRS.2013.2287017.

Snyder, J., H. Bluestein, and G. Zhang, 2010: Attenuation correction and hydrometeor classification of high-resolution, X-band, dual-polarized mobile radar measurements in severe convective storms. *J. Atmos. Oceanic Technol.*, **27**, 1979–2001, https://doi.org/10.1175/2010JTECHA1356.1.

Testud, J., E. L. Bouar, E. Obligis, and M. Ali-Mehenni, 2000: The rain profiling algorithm applied to polarimetric weather radar. *J. Atmos. Oceanic Technol.*, **17**, 332–356, https://doi.org/10.1175/1520-0426(2000)017<0332:TRPAAT>2.0.CO;2.

Trabal, J. M., E. Gorgucci, V. Chandrasekar, and D. J. McLaughlin, 2014: Evaluation of the self-consistency principle for calibration of the CASA radar network using properties of the observed precipitation medium. *IEEE Trans. Geosci. Remote Sens.*, **52**, 149–162, https://doi.org/10.1109/TGRS.2012.2237406.

Trömel, S., M. R. Kumjian, A. V. Ryzhkov, C. Simmer, and M. Diederich, 2013: Backscatter differential phase—Estimation and variability. *J. Appl. Meteor. Climatol.*, **52**, 2529–2548, https://doi.org/10.1175/JAMC-D-13-0124.1.

Unal, C., 2009: Spectral polarimetric radar clutter suppression to enhance atmospheric echoes. *J. Atmos. Oceanic Technol.*, **26**, 1781–1797, https://doi.org/10.1175/2009JTECHA1170.1.

Vulpiani, G., M. Montopoli, L. D. Passeri, A. G. Gioia, P. Giordano, and F. S. Marzano, 2012: On the use of dual-polarized C-band radar for operational rainfall retrieval in mountainous areas. *J. Appl. Meteor. Climatol.*, **51**, 405–425, https://doi.org/10.1175/JAMC-D-10-05024.1.

Wang, Y., and V. Chandrasekar, 2009: Algorithm for estimation of the specific differential phase. *J. Atmos. Oceanic Technol.*, **26**, 2565–2578, https://doi.org/10.1175/2009JTECHA1358.1.

——, and ——, 2010: Quantitative precipitation estimation in the CASA X-band dual-polarization radar network. *J. Atmos. Oceanic Technol.*, **27**, 1665–1676, https://doi.org/10.1175/2010JTECHA1419.1.